Structural details in Li3PS4: Variety in thiophosphate building blocks and correlation to ion transport

Omer Ulas Kudu, Theodosios Famprikis, Sorina Cretu, Benjamin Porcheron, Elodie Salager, Arnaud Demortière, Matthieu Courty, Virginie Viallet, Thierry Le Mercier, Benoit Fleutot, et al.

Overlooked structural details in ball-milled Li_3PS_4: variety in thiophosphate building blocks and correlation to ion transport

Ömer Ulaş Kudu [a,d*], *Theodosios Famprikis* [a,c], *Sorina Cretu* [a], *Benjamin Porcheron* [b,e], *Elodie Salager* [b,e], *Arnaud Demortiere* [a], *Matthieu Courty* [a,b], *Virginie Viallet* [a,b], *Thierry Le Mercier* [d], *Benoit Fleutot* [a,b], *Marc-David Braida* [d], *Christian Masquelier* [a,b,c*]

[a] Laboratoire de Réactivité et de Chimie des Solides (UMR CNRS 7314), Université de Picardie Jules Verne, 33 rue Saint Leu, 80039 Amiens Cedex, France

[b] Réseau sur le Stockage Électrochimique de l'Énergie (RS2E), FR CNRS 3459, 80039 Amiens, France

[c] ALISTORE European Research Institute, FR CNRS 3104, 80039 Amiens Cedex, France

[d] Solvay R&I, 52 rue de la Haie Coq, 93306 Aubervilliers, France

[e] CNRS, CEMHTI UPR 3079, Université d'Orléans, Orléans, France

***Corresponding Authors**

ulaskudu@gmail.com (U.K.)

christian.masquelier@u-picardie.fr (C.M.)

Abstract

Li_3PS_4 is an attractive solid-electrolyte material that possesses high RT ionic conductivity (10^{-4} $S.cm^{-1}$) but the effects of specific synthesis parameters on the material's local structure and transport properties still demand clarifications. Herein, we highlight the substantial effects of cooling breaks in the mechanochemical synthesis procedure on the formation of a variety of $P_xS_y^{a-}$ moieties and on the transport properties of Li_3PS_4, through Raman and impedance spectroscopy measurements. We show that ball-milled Li_3PS_4 (with no subsequent annealing), which is often regarded as "amorphous/glass/glassy Li_3PS_4", is not fully amorphous using X-ray diffraction and transmission electron microscopy. Upon subsequent annealing for 1 hour above 190 °C, β-Li_3PS_4 is crystallized and our ^{31}P magic angle spinning nuclear magnetic resonance spectra suggest that 3 distinct PS_4^{3-} moieties form, which we refer to as amorphous-, β- and ϒ-type units. Herein, we present a hypothesis to explain the correlation between the ionic conductivity and the distinct PS_4^{3-} units as a function of the annealing temperature. Our results consolidate the recent reports noting that crystallization of β-Li_3PS_4 is not necessary to obtain a high conductivity in ball-milled Li_3PS_4. Finally, we introduce a phase mixture between β-Li_3PS_4 and ϒ-Li_3PS_4 synthesized at 200 °C, which is the lowest synthesis temperature yet for ϒ-Li_3PS_4.

Keywords: Ball-milling, β-Li_3PS_4, ϒ-Li_3PS_4, ^{31}P MAS NMR, Raman, Conductivity

Introduction

Solid Li^+ (Na^+) conductors in the Li_2S (Na_2S) – P_2S_5 binary system have received a lot of attention as they have the potential to replace liquid electrolytes from the conventional Li (Na) - ion batteries [1–7]. In particular, Li_3PS_4 has been the subject of many studies owing to its low cost and relatively high ionic conductivity (~10^{-4} S.cm^{-1}) at room temperature (RT). The precise correlation between the synthesis parameters and the ionic conductivities obtained for different samples of Li_3PS_4 still remains to be better addressed [7–14].

Li_3PS_4 has been isolated as four known crystalline polymorphs, β, ϒ, α and δ, the last of which being obtained at high pressure (>5 GPa) [8,12,14–19]. ϒ-Li_3PS_4, which is formed from a solid-state reaction between 75 mol% Li_2S and 25 mol% P_2S_5 at high temperature (500 – 900 °C), possesses a poor RT conductivity of around 10^{-7} S.cm^{-1} [8,9,20]. When ϒ-Li_3PS_4 is heated between ~280 °C and ~500 °C, it transforms into β-Li_3PS_4, referred to as "bulk β-Li_3PS_4". Above ~500 °C, β-Li_3PS_4 turns into α-Li_3PS_4. Upon cooling α-Li_3PS_4 back to RT, it transforms into ϒ-Li_3PS_4 at around 270 °C and β-Li_3PS_4 is not observed [14,17]. The phase transformations in Li_3PS_4 are summarized in **Figure 1a**. Even though ϒ-Li_3PS_4 is the equilibrium RT phase [14,19,21], different metastable phases can also be stabilized at RT, as summarized in **Figure 1b**.

The extrapolation of the high temperature ionic conductivity of bulk β-Li_3PS_4 to RT results in ~10^{-6} S.cm^{-1} [8,9,14,16]. Interestingly, this value can be enhanced substantially (~10^{-4} S.cm^{-1}) if β-Li_3PS_4 is stabilized at RT through two different synthesis routes summarized in **Figure 1b**:

i. A mechanochemical reaction between stoichiometric amounts of Li_2S and P_2S_5 through ball-milling leads to the formation of a material that is identified as mostly amorphous through X-ray diffraction. β-Li_3PS_4 forms after annealing the ball-milled mixture between 180 and 250 °C and it remains stable at RT [10,12,13].
ii. Reacting stoichiometric amounts of Li_2S and P_2S_5 in an organic solvent (THF, DME, ACN etc.) and subsequently drying the mixture between 140 – 200 °C under vacuum yields β-Li_3PS_4, which is stable at RT [16,20,22–28].

Ball-milling the reagents without a subsequent annealing step results in X-ray amorphous Li_3PS_4 [2,5,10,13,29,30], which possesses quite similar transport properties with RT-stabilized β-Li_3PS_4 (through mechanochemical or wet-chemistry routes). Both materials have RT conductivities of ~10^{-4} S.cm^{-1} and activation energies between 0.36 – 0.38 eV, the reasons of which have not been explained [7]. The recent studies of Smith et al. [31] and Kaup et al. [14] suggest that the rotational dynamics of the anions (PS_4^{3-}) in amorphous and β-Li_3PS_4 could be responsible for their high conductivities, which could also play a role in their afore-mentioned similarity. Other recent studies showed that when X-ray amorphous Li_3PS_4 is annealed around 180 °C, β-Li_3PS_4 is crystallized and a further increase in the annealing temperature leads to a gradual decrease in the material's conductivity, which raises questions over the transport properties of β-Li_3PS_4 [10–13,32–34].

In this article, we focus on the mechanochemical route used to synthesize X-ray amorphous- and β-Li_3PS_4. First, we show how the absence of cooling breaks during the initial cycles of ball-milling could alter the local structure of X-ray amorphous Li_3PS_4 and decrease its ionic conductivity by using X-ray diffraction (XRD), Raman and impedance spectroscopies. We then report on the presence of nanocrystallites in X-ray amorphous Li_3PS_4, which are invisible to

powder X-ray diffraction, identified by transmission electron microscopy (TEM). We also try to explain the inverse correlation between the ionic conductivity and the synthesis temperature of β-Li_3PS_4 by synthesizing a series of samples and investigating their crystallite sizes and their local phosphorus environments. Using ^{31}P magic-angle-spinning nuclear magnetic resonance spectroscopy (^{31}P MAS NMR), we identified 3 distinct PS_4^{3-} environments simultaneously co-existing in β-Li_3PS_4, which could be responsible for the afore-mentioned correlation. Finally, we present a phase mixture of β-Li_3PS_4 and ϒ-Li_3PS_4, which could be a promising solid electrolyte owing to its potentially higher electrochemical and moisture stabilities.

Experimental

Synthesis: Mechano-chemical syntheses (planetary ball-milling) were carried out using a Retsch PM200 and a Fritsch Pulverizette 7 apparatus using the reagents Li_2S (Sigma Aldrich) and P_2S_5 (Sigma Aldrich). The preparation of the ball milling jars took place in an Ar-filled glovebox. 5 g of stoichiometric mixtures were put in 45 mL zirconia jars along with 15 zirconia balls with 10 mm diameters (3 g each). The jars were sealed using scotch tape and parafilm, then they were taken out of the glovebox and placed in the ball milling apparatus. For intermittent ball-milling, cycles of 15 minutes of milling and 15 minutes of break; for continuous ball-milling, cycles of 30 minutes were programmed. The rotation direction was reversed between each milling cycle. In all the syntheses, a rotation speed of 510 RPM was used. After milling, the jars were carried back to an Ar-filled glovebox and opened inside. The powder was pale yellow and was mostly stuck on the balls. Some glassy depositions were also observed on the jar walls, which was thicker in the cases of continuous milling. For annealing, pelletized samples (at 531 MPa) were placed in the C-coated quartz tubes in an Ar filled glovebox, the tubes were sealed with parafilm before they were taken out. The tubes were then connected to a pump that generates primary vacuum using a Swagelok quick-connection

apparatus and were sealed under vacuum. We tried to keep the sealing process as short as possible to prevent the heat to affect the reaction pellets. The sealed ampoules and the pellets were then put in furnaces, heated up to the reaction temperatures via 5 °C/min heating rate. After the reactions were completed, the tubes were left in the oven and cooled down to RT slowly, then were placed in an Ar-filled glovebox in which they were opened and the pellet was ground using an agate mortar and pestle.

Powder X-ray Diffraction. The powder X-ray diffraction patterns were collected using Bruker D8 diffractometers equipped with either Co ($K\alpha_1$-$K\alpha_2$) or Cu ($K\alpha_1$-$K\alpha_2$) radiation in a θ-θ configuration. Since the samples were air-sensitive, they were sealed in hermetic sample holders which were capped by a Be window in an Ar-filled glovebox. The patterns were collected between $2\theta = 10° - 60°$ or $10° - 100°$ for 1 hour or 13 hours, respectively, in which a stepsize of 0.03° was used. The Fullprof suite was used to perform profile matching using Le Bail method to determine the lattice parameters of the samples.

Raman Spectroscopy. The samples for Raman spectroscopy were prepared in an Ar-filled glovebox as follows: a small quantity of powder was put on a glass slide and it was sealed with scotch tape, then the lamellas were taken out and their spectra were measured quickly. The spectra were collected using a Raman DXR Microscope (Thermo Fischer Scientific) with excitation laser beam wavelength of 532 nm and a low laser power of 0.1 mW to prevent excessive heating of the samples. The samples were exposed to the beam in a series of 100 measurements of 1 second exposure each to collect the spectra. The data were deconvoluted using Omnic Software of Thermo Fischer Scientific and used a pseudo-Voigt function for fitting.

^{31}P Magic Angle Spinning Nuclear Magnetic Resonance Spectroscopy. The samples were packed in 4 mm rotors in an Ar-filled glovebox and sealed by a KEL-F cap. The (β+ϒ)-Li_3PS_4 samples were measured in a 7 T Bruker Avance III spectrometer operating at 162.08 MHz for ^{31}P, in which they were spun at 7.5 kHz under dry nitrogen gas using a Bruker 4mm double resonance HX probe. The one pulse spectra were collected and analyzed using a direct RF impulsion of 3.125 us (80 kHz). The spectra for the 84 hour-200°C annealed sample was measured with a recycling time of 500 s using 8 scans and the 336 hour-200°C annealed sample in 4 scans with a recycling time of 450 s (more than 5 times the longest measured longitudinal relaxation time). The remaining samples were studied in a 400 MHz wide bore Neo Bruker spectrometer operating at 162.08 MHz for ^{31}P in which they were spun at 10 kHz. The one pulse ^{31}P-MAS NMR spectra were collected and analyzed in direct impulsion using either 90° pulse length of 4.5us with a recycling time of 500s in 8 scans or a 90° pulse length of 3.33us with a recycling time of 300s in 8 scans. All the spectra were referenced to H_3PO_4 (0 ppm). The fits of the spectra were done with the ssNake software [35]. The spectra of the as ball milled and 150 °C-annealed samples were fitted with 3 Gaussian components. For the samples annealed above 200 °C, the fit was done with 3 Voigt peaks for the PS_4^{3-} units and 2 Gaussian peaks for the $P_2S_7^{4-}$ units. The values of the shifts were parameters of the fit, but the set of chemical shifts was constrained to be identical over the 5 samples. The Lorentzian and Gaussian widths were left free to evolve, and set to zero whenever they were below 10 Hz. The contributions of spinning sidebands were ignored as they did not modify the relative quantities of each peak significantly (similar anisotropies).

Differential Scanning Calorimetry. About 10 mgs of samples were placed in aluminum crucibles in an Ar filled glovebox before the crucibles were sealed, then their lids were pierced under argon flow prior to the measurement to allow gas release upon heating. A Netzsch DSC

204 F1 heat flux differential calorimeter was used for the measurements, in which the samples were heated with a rate of 5 °C.min^{-1} under a constant argon flow of 50 mL.min^{-1}. The enthalpy of the thermal phenomena were measured by the software Proteus Analysis.

Transmission Electron Microscopy. TECNAI F20 S-TWIN (ThermoFisher) operating at 200 kV was used for performing transmission electron microscopy analyses. BM-I Li_3PS_4 powders were dispersed on an ultrathin carbon coated copper grids in a glovebox (Ar atmosphere). The TEM holder containing the sample was sealed in a nylon bag full of Ar atmosphere in the glovebox to protect the sample from moisture and was transferred to the TEM column. An argon flowing pipe was placed near to the holder to minimize sample reaction with air while the sample was transferred from the nylon bag to the TEM column in less than 5 seconds. As the material is highly sensible to the electron beam during the TEM measurements, the electron dose was minimised by using a smaller condenser aperture (10 µm) and a higher spot size (6).

Alternating Current Impedance Spectroscopy. We cold-pressed our samples into 6-mm diameter pellets and stacked them between carbon (graphite) electrodes directly in the press at 531 MPa. We controlled the experiment temperature using an Intermediate Temperature System furnaces (Biologic Company, ITS). We recorded the AC impedance spectra of our samples using a MTZ 35 frequency response analyzer (BioLogic Company) between the frequency range from 30 MHz to either 1 Hz or 100 mHz with an excitation signal of 50 mV. We treated the impedance data using Zview software and Debye model equivalent circuit (see SI for more information) to differentiate different resistive phenomena and to obtain their resistance. Ionic conductivity values were calculated as explained in a previous study [36]

using resistance values obtained from the fits. To calculate the capacitance values of different resistive phenomena at various temperatures, we used the equation:

$$R\ x\ C = \frac{1}{2\ x\ \pi\ x\ f_c}$$

In the equation, R, C and f_c stand for resistance, capacitance and frequency cut, respectively. The method to obtain the frequency cut of a phenomenon at different temperatures was explained in a previous study in detail [36].

Results and Discussion

Ball-milled Li_3PS_4 with no subsequent heat treatment is often referred to as "amorphous" or "glass" or "glassy" Li_3PS_4 and manifests a halo powder XRD pattern [5,10,12,29,30,37,38]. On the other hand, Dietrich et al. suggest that Li_2S cannot be fully amorphized during the synthesis [2]. This apparent discrepancy could arise from the sensitivity of the XRD measurements or from some differences between the ball-milling parameters [39], one of which is having cooling breaks in between ball-milling cycles Advanced 7Li NMR studies are also highly needed if one really cares about determining exact Li_2S contents. A few reports emphasize the importance of these breaks for obtaining an impurity-free product, which remained to be proven experimentally [2,7,40]. We used two reaction pathways to synthesize BMed Li_3PS_4, by which we can differentiate the effect of cooling breaks at the early stages of the mechanochemical reaction. The first one (BM-I) refers to Li_3PS_4 synthesized by intermittent ball-milling (BM-I), i.e 76 hours overall for 38 hours of ball-milling and 38 hours of cooling breaks every 15 minutes. The second one (BM-C) refers to Li_3PS_4 synthesized by continuous ball-milling, i.e. 22 hours of continuous ball-milling followed by 38 hours overall of ball-milling + cooling breaks every 15 minutes (41 hours of active milling). We assumed that the impurities (identified by Raman spectroscopy) would form during the initial continuous

ball-milling. The additional intermittent ball-milling was done to equilibrate the overall active ball-milling time and to have similar degrees of amorphization in the samples.

The XRD patterns of the two ball-milled samples are shown in **Figure 2a**, which indicates that our ball-milling recipe, with or without the cooling breaks, yields a composite of an X-ray amorphous matrix and residual Li_2S [41]. Due to the residual Li_2S, we expect the overall compositions of the amorphous matrices to be $Li_{3-2x}PS_{4-x}$ and point out that these materials should not be labelled as "amorphous/glass/glassy Li_3PS_4". "Ball-milled Li_3PS_4" would be a more fitting definition as it indicates the overall composition of the material and the process that it went through.

As shown in **Figure 2b**, the Raman spectra of BM-I and -C Li_3PS_4 look qualitatively very similar. As reported by Dietrich et al. [2], deconvoluting the frequency range between 440 and 360 cm^{-1} in these spectra gives quantitative information about the $P_xS_y^{a-}$ units in these materials within ~5% error margin. Doing that, we show that BM-I Li_3PS_4 has a very high relative quantity of PS_4^{3-} along with some $P_2S_7^{4-}$ and $P_2S_6^{4-}$ moieties, similar to what is reported in the literature [2,8,37,42–47] . The presence of $P_2S_7^{4-}$ and $P_2S_6^{4-}$ moieties can be explained by the incomplete reaction between the reagents, which is evidenced by the residual Li_2S. BM-C Li_3PS_4 has comparatively higher amounts of $P_2S_7^{4-}$ and $P_2S_6^{4-}$ moieties and there is also a noticeable shift in the peak position of $P_2S_7^{4-}$. Such shifts are expected in amorphous Li_2S – P_2S_5 materials, in particular depending on the relative molar ratios of the reagents [2]. We hypothesize that the heat generated during continuous ball-milling may cause sulfur (or reagent) evaporation [2]. Such difference between the two samples could originate from the absence of cooling steps during the synthesis of BM-C Li_3PS_4. Reactants and intermediate products with low sublimation temperatures (i.e. P_2S_5, P_xS_y, S_x^{b-} etc.) may sublimate due to

overheating and alter the reaction dynamics during ball-milling. To the best of our knowledge, there are no $P_xS_y^{a-}$ units demonstrating bond vibrations centered at 402 and 433 cm^{-1}, so these signals may originate from elemental sulfur (S_8), some polysulfide species (S_x^{2-}) or some exotic $P_xS_y^{a-}$ units [48–50], which may deteriorate the performance of an electrolyte in a battery.

Figures 3a (zoomed in at the high frequency region) and **3b** (zoomed out) show the Nyquist plots of BM-I and -C Li_3PS_4 recorded at -20 °C. Semicircles at the high frequency region (30 MHz – 0.7 kHz) indicate similar ionic conduction behaviour for both samples. As frequently done in the literature to determine the ionic resistance of a pellet, if the linear tails following the semicircles shown in Figure 4a are extrapolated to the x axis (real resistance), similar resistance values are obtained for BM-I and -C Li_3PS_4. However, a zoomed out view on the same Nyquist plots shows the presence of a second semicircle in BM-C Li_3PS_4, which signals a second resistive phenomenon, see **Figure 3b**. These observations are confirmed in the Bode plots of the two materials at the same temperature, as shown in **Figures 3c** and **3d**, which points out the importance of a careful investigation on impedance data in a wide frequency window (typically 1 Hz – 1 MHz) [51,52]. The real resistance of the BM-I Li_3PS_4 pellet was obtained by fitting the impedance data using a Debye equivalent circuit (**Figure S1** [53]). Based on BM-C Li_3PS_4's Raman data, we hypothesize that the material has a core-shell structure as illustrated in **Figure 4a**. At the initial stages of ball-milling, the reaction between Li_2S and P_2S_5 proceeds as expected [2] and the core of the new product particle is formed. As the accumulated heat increases the temperature, some of the reagents and/or intermediate products (i.e. P_2S_5, P_xS_y, S_x^{b-} etc.) gets sublimated and alter the reaction dynamics, hence some impurities form at the shell. Li^+ moves through the shell and then the core subsequently, which could be modelled with a slightly modified Debye equivalent circuit as in **Figure S1** [53].

The Arrhenius plots gather the conduction behaviour in BM-I and -C Li_3PS_4, see **Figure 4b**. BM-I Li_3PS_4 has a conductivity of 4.10^{-4} $S.cm^{-1}$ at RT and an activation energy of 0.37 eV, which are comparable to the values found in the literature [2,5,10,13,29,30]. The 1st conductive medium in BM-C Li_3PS_4 shows quite a similar resistance to BM-I Li_3PS_4, hence we associate this medium with the hypothesized core that consists of PS_4^{3-} units. The 2nd medium demonstrates a higher resistance (leading to an observable conductivity of ~10^{-5} $S.cm^{-1}$ at RT), which lowers the total conductivity of BM-C Li_3PS_4 dramatically (2.10^{-5} $S.cm^{-1}$ at RT). Among the amorphous Li_2S – P_2S_5 materials, the ones with relatively higher PS_4^{3-} content have higher conductivities than the ones mostly composed of $P_2S_7^{4-}$, $P_2S_6^{4-}$ and PS_3^- [2,5,29]. Thus, we associate the poorly conductive 2nd medium to the impurity phases in the hypothesized shell of BM-C Li_3PS_4. Additionally, it is worth pointing out that the capacitance values of the 1st and the 2nd phenomena were calculated as a function of temperature, as shown in **Figure 4c**. The frequencies of these phenomena shift to higher values with increasing temperature, but their capacitances remain stable, which proves that they originate from a different conductive medium.

The investigation of BM-I Li_3PS_4 using transmission electron microscopy (TEM) was carried out with low dose conditions (below few hundred $e^-/nm^2/s$) and proper exposition time in order to minimise the electron beam damage which is mainly required for these sensitive materials [54]. **Figure 5a** displays predominant grains of BM-I Li_3PS_4 which exhibit no specific morphology with the size of a few micrometers. Based on SAED measurements (Selected Area Electron Diffraction), the diffraction pattern showed diffused rings related to an amorphous phase. Furthermore, some nanosized particles (30-100 nm) spread out in the amorphous matrix can be observed by contrast as shown in **Figure 5b**. As displayed in **Figure 5c**, crystalline particles from 15 to 250 nm are present inside an amorphous matrix. The SAED pattern in

Figure 5d reveals the crystallinity of objects inside the amorphous matrix, that consisted in a mixture of Li_2S traces [41] and some other products of reaction between Li_2S and P_2S_5. The crystallites presented in our amorphous matrix could be similar as the ones reported previously by Tsukasaki et al. using in-situ TEM where they investigated a ball-milled Li_3PS_4 sample (no subsequent annealing) [38]. They suggested that the nanocrystallites could contribute to the high ionic conductivity of the material [10,38], but we argue that it might be unlikely since the crystallites are scarce and well-separated. BM-I Li_3PS_4 having high PS_4^{3-} content and similar conductivity to the literature values, we hence used it as the precursor to study the formation of β-Li_3PS_4.

Rise of β-Li_3PS_4 and fall of conductivity. β-Li_3PS_4 is the medium temperature polymorph of Li_3PS_4, which is thermodynamically stable in the range 280 – 500 °C, and has an extrapolated RT conductivity of ~10^{-6} $S.cm^{-1}$ [8,9,14,16]. When it is stabilized at RT through a mechanochemical reaction between Li_2S and P_2S_5, and a subsequent annealing between 180 and 250 °C, an increase of two orders of magnitude is observed in its RT conductivity (~10^{-4} $S.cm^{-1}$), which is substantially similar to the RT conductivity of X-ray amorphous Li_3PS_4 (also ~10^{-4} $S.cm^{-1}$ [2,5,10,13,29]). In an effort to understand the causes of this similarity, we decided to carefully investigate the changes in the ionic conductivity, in the variety of $P_xS_y^{a-}$ units present and in the XRD patterns of X-ray amorphous Li_3PS_4, as a function of annealing temperature.

The differential scanning calorimetry (DSC) data of BM-I Li_3PS_4 is shown in **Figure 6a**. The baseline with constant slope indicates that the material doesn't go through any detectable reaction until 160 °C. At higher temperatures, the reactions can be divided into 3 regions: (i) an exothermic reaction between 165 – 202 °C, (ii) another exothermic reaction between 202 –

230 °C and (iii) a set of endothermic reactions between 230 – 315 °C. To observe the possible changes in the local and crystal structure of BM-I Li_3PS_4 before, during and after these reactions, we then annealed a set of samples separately at various temperatures (marked on **Figure 6a)** for **1 hour** (each sample at a temperature), subsequently cooled down to RT. For ease of notation, we will refer to these samples as "Annealing temperature-Li_3PS_4" (i.e. BM-I Li_3PS_4 annealed at 150 °C for 1 hour is 150-Li_3PS_4).

The XRD pattern of BM-I Li_3PS_4 suggests that it is a composite of an X-ray amorphous matrix and residual Li_2S. The XRD patterns of the composite when it is annealed between 150 °C and 180 °C do not change much, as illustrated in **Figure 6b**. The sample starts to crystallize at 180 °C, as evidenced by the broad peaks with very low intensities. The relative intensities of the Li_2S diffraction peaks gradually decrease as the annealing temperature increases, which indicates that the residual Li_2S reacts with the X-ray amorphous matrix at these temperatures and increases the Li and S contents in the matrix. In **190**-Li_3PS_4, β-Li_3PS_4 is crystallized (Pnma, see **Figures 7** and **S2**, and **Table 1** for lattice parameters). The diffuse scattering in the same pattern signals the presence of an additional X-ray amorphous phase, the relative intensity of which monotonically decreases with increasing annealing temperature whereas the diffraction peaks become sharper as the annealing temperature increases.

Interestingly, the (101), (111) and (121) Bragg reflections are not obviously visible in the patterns of 190- and 202-Li_3PS_4 and their relative intensities monotonically increase with the annealing temperature, the reason of which being not clear to us. In some studies the term "thio-lisicon III analogue" [55] was used to describe the crystal structure of Li_3PS_4 samples [27,38,56–62], which shared similar features as 190- and 202-Li_3PS_4. Perhaps the low

intensities of (1k1) reflections was the reason why the phases were not indexed using the Pnma space group.

Table 1: (single column) Lattice parameters of BM-I Li_3PS_4 annealed at 190, 202, 230 and 315 °C for 1 hour and samples from the literature, which were crystallized into the Pnma space group. TW, WC, and BMβ stand for "This Work", β-Li_3PS_4 synthesized through "Wet Chemistry", and β-Li_3PS_4 synthesized through "Ball-Milling" and subsequent annealing, respectively.

Sample	Anneal Temp. (°C)	Lattice Parameters (Å)			Domain size (Å)
		a	b	c	
TW	190	12.93(1)	8.09(1)	6.11(1)	475(1)
TW	202	12.90(1)	8.10(1)	6.12(1)	684(1)
TW	230	12.90(1)	8.16(1)	6.14(1)	>1000
TW	315	12.91(1)	8.14(1)	6.14(1)	>1000
WC [16]	140	12.99	8.06	6.14	?
BMβ [12]	250	12.88	8.14	6.15	?

The lattice parameters of the crystalline samples are shown in **Table 1**. There is a general trend of slightly decreasing *a* and increasing *b* and *c* parameters with increasing the annealing temperature. Interestingly, the lattice parameters of "nanoporous" β-Li_3PS_4 synthesized through wet chemistry (WC-Li_3PS_4) [16] are substantially different than the ones of our samples and the ones of β-Li_3PS_4 synthesized through ball-milling and subsequent annealing at 250 °C (BMβ-Li_3PS_4) [12]. WC-Li_3PS_4 crystallizes at relatively lower temperatures than BMβ-Li_3PS_4, which could be due to the difference in their particle sizes [7], hence the differences in their lattice parameters might be justified by the trend between the annealing temperature and the lattice parameters as mentioned above.

We investigated the changes in the $P_xS_y^{a-}$ units in BM-I Li_3PS_4 upon annealing using quantitative ^{31}P MAS NMR. As shown in **Figure 8**, BM-I Li_3PS_4 is rich in PS_4^{3-} species with

a broad Gaussian peak centred at 83.2 ppm. The fits are not heavily constrained, but our best fit indicates that these PS_4^{3-} units account for 81% of the relative signal area, whereas impurities in the $P_2S_6^{4-}$ and $P_2S_7^{4-}$ range (90 – 110 ppm [2]) add up to 19% of the signal, in coherence with the results obtained by Raman spectroscopy (**Figure 2b**). The component centered at 93 ppm is extremely broad and signals a wide distribution of environments in the impurities resulting from the ball-milling process. Annealing at 150°C does not change dramatically the spectrum but narrows the distribution of impurities and decreases their signal to 14%, in agreement with the hypothesis of a reaction between the amorphous matrix and the Li_2S that remained after the mechanochemical reaction. This reaction can introduce terminal sulfur atoms to the $P_2S_6^{4-}$ and $P_2S_7^{4-}$ species and facilitate the formation of PS_4^{3-} [2]. After the onset of crystallization of β-Li_3PS_4, the NMR spectra of the Li_3PS_4 samples change dramatically, as can be seen in **Figure 8b.** The broad PS_4^{3-} peak at 83.2 ppm changes into a new intense resonance at 86.4 ppm. A downfield shoulder around 88.6 ppm is clearly present in 202-Li_3PS_4, and is reduced with increasing annealing temperature. An additional broad component in the low-ppm side provides a better fit in 202-Li_3PS_4 (see below). Variations in the ^{31}P chemical shift of PS_4^{3-} moieties were previously observed in ^{31}P spectra of Li_3PS_4. Gobet et al. indeed studied the $Li_3PS_4 \cdot 3THF$ phase that displayed three peaks between 86.8 and 89.6 ppm, all assigned to PS_4^{3-}. The differences in shifts were assigned to "molecular-scale variations", i.e. varying THF configurations [20]. The desolvated phase resulted in a single broad Gaussian peak centered at 83.9 ppm. Stoffler et al. assigned the broad components under the sharp 86.5 ppm peak to an amorphous phase with a relatively high quantity (30%), assigned to PS_4^{3-} moieties [18]. Phuc et al. assigned the fitted peaks located at 81.5, 83.6 and 85.7 ppm to PS_4^{3-} species in amorphous, β- and ϒ-Li_3PS_4 when they studied 100 $Li_3PS_4.xLi_3PO_4$ materials [63].

We attempted to fit the NMR spectra to interpret the evolution with annealing time. A better fit of the centerband of 202-Li_3PS_4 was obtained with three peaks. The chemical shift anisotropies are small, similar and do not influence significantly the relative amounts obtained from the fits; they were therefore neglected. The fit was not strongly constrained however, and the contribution of each peak to the total spectrum, as well as its position, was ill-defined with several equivalent outputs. We therefore decided to fit simultaneously the spectra of all the crystallized samples. We used ssNake [35] with 3 Voigt peaks for the PS_4^{3-} region and two Gaussian peaks for the impurities between 93 and 97 ppm. ssNake allows for optimizing the set of chemical shifts that fit best all the spectra simultaneously. The Gaussian and Lorentzian widths as well as the intensities were left free to optimize, except when the values went below 10 Hz for the widths (set to zero and fixed afterwards). These constraints produced reasonable fits, with the resulting high-ppm shifts (86.4 and 88.6 ppm) in good agreement with the reported peak positions for PS_4^{3-} units in β-Li_3PS_4 (83.9 – 86.5 ppm [18,20]) and ϒ-Li_3PS_4 (88.2 – 88.4 ppm [20,64]). The third additional peak has a relatively smaller chemical shift (85.9 ppm). A worse agreement of the fit was obtained for 315-Li_3PS_4 compared to the four other samples, which was solved by removing the 88.6 ppm and adding another peak at 89.2 ppm. We also tried fitting all the spectra simultaneously with 2 Voight peaks for the PS_4^{3-} region for comparison, which produced less accurate fits. The fitting parameters for these attempts are shown in **Table S4**, and the fits are shown in **Figures S3**.

Table 2: (single column) Relative quantities of PS_4^{3-} units (obtained from a fit, see **Table S2**) as a function of the annealing temperature of BM-I Li_3PS_4. **A.-type** and **PS_4^{3-} Rel. Qty.** are the abbreviations of amorphous-type and PS_4^{3-} relative quantities, respectively. *The third peak in 315-Li_3PS_4 is centred at 89.1 ppm for a significantly better agreement. Any difference from 100% arises from a small amount of impurities.

Anneal Temp (°C)	PS_4^{3-} Rel. Qty. (%)		
	A.-type (85.9 ppm)	β-type (86.4 ppm)	ϒ-type (88.6 ppm)

202	16	66	17
230	11	80	9
315	12	80	7*

We therefore assign the peaks at 86.4 and 88.6 ppm to the PS_4^{3-} units in β- and ϒ-Li_3PS_4, respectively, due to the similarity with the reported values [18,20,63,64]. The position of the peak at 85.9 ppm is closest to the resonance of PS_4^{3-} moieties in β-Li_3PS_4. We hypothesize that this peak originates from the PS_4^{3-} units that are located at the domain boundaries of β-Li_3PS_4, which are more disordered and more dynamic in a similar fashion to the ones in BM-I Li_3PS_4. Due to this similarity, and for simplicity, we will refer to these units as *amorphous-type* PS_4^{3-}, and the aforementioned two other as *β-* and *ϒ-type* PS_4^{3-}. The small peaks between 93 and 97 ppm are assigned to $P_2S_7^{4-}$ impurities [2,40,65]. They add up to less than 1% of the total signal. and were neglected in the percentages given in the following. They did not change significantly the relative importance of the units in the main signal. The relative quantities of these PS_4^{3-} moieties change notably with increasing annealing temperature, see **Table 2**. There is a significant amount (16%) of amorphous-type PS_4^{3-} in 202-Li_3PS_4 but their relative quantity decreases to 11-12% at higher annealing temperatures (230 and 315 degrees). Interestingly, while the amount of amorphous-type PS_4^{3-} does not change significantly between 230- and 315-Li_3PS_4, the shape of the NMR peak for amorphous-type PS_4^{3-} goes from mixed Gausso-Lorentzian to narrower and exclusively Gaussian in 315-Li_3PS_4. This narrowing hints at faster dynamics and probably some structural reorganization upon higher annealing temperatures [66]. The XRD data of the β-Li_3PS_4 samples reveal that their coherently scattering domain sizes increase with their annealing temperatures (see **Table 1**), hence their domain boundary areas decrease. We hypothesize that the amorphous-type unit contents decrease in 230-Li_3PS_4 is due to a sharp decrease in boundary areas. The relative quantity of ϒ-type units also decreases with increasing the annealing temperature to 230°C. It suggests that the ϒ-type units transform into

β-type units, as observed for ϒ-Li_3PS_4 for annealing temperatures above 280°C [8,9]. At 315°C, the amount of ϒ-type units decreases slightly within our uncertainty. More interestingly its shift is modified to 89.1 ppm, indicating a local structural change in these environments.

The RT ionic conductivity of BM-I Li_3PS_4 is 4.10^{-4} $S.cm^{-1}$, which is similar to the conductivity of "amorphous/glass/glassy" Li_3PS_4 reported in the literature [2,5,10,13,29,30]. In **Figure 9**, the evolution of the RT ionic conductivity as a function of the annealing temperature (for 1 hour) is shown in comparison with the study of Tsukasaki et al. [10]. Our data, in agreement with [10], show 2 clear trends: (i) the conductivity increases when the annealing temperature is lower than or equal to 180 °C and (ii) the conductivity decreases if the sample is annealed above 180 °C. The XRD patterns and the ^{31}P NMR spectra of the BM-I Li_3PS_4 samples annealed up to 180 °C show that the relative diffraction peak intensities of Li_2S and the relative quantities of the impurities ($P_2S_7^{4-}$ and $P_2S_6^{4-}$) were decreased, which suggests that the residual Li_2S reacts with the matrices upon annealing. This reaction increases the relative quantity of PS_4^{3-} and the charge carrier (i.e. Li^+) concentration in the amorphous matrix, which could be the reason of the increase in the conductivity until 180 °C. A cold-pressed pellet of 180-Li_3PS_4 has a RT ionic conductivity of 9.10^{-4} $S.cm^{-1}$, which is comparable to the RT conductivity of a cold-pressed pellet of $Li_7P_3S_{11}$ (10^{-3} $S.cm^{-1}$ [67]).

β-Li_3PS_4 crystallizes at 190 °C and the material's RT conductivity is reduced significantly. The conductivity continues to decrease with increasing annealing temperature and was finally measured as 8.10^{-5} $S.cm^{-1}$ in 315-Li_3PS_4, which consolidates the previous reports pointing out that the decrease in the conductivity of "amorphous" Li_3PS_4 is observed upon crystallization of β-Li_3PS_4 [10–13,32–34]. Our results point therefore towards a monotonous increase in ionic conductivity with the relative quantity of "*amorphous-type PS_4^{3-} units*" and with decreasing

domain size of β-Li_3PS_4 (see **Table 2** and **Figure 10**). Higher RT conductivities can be obtained in samples consisting of relatively more disordered and presumably more dynamic PS_4^{3-} anions (in this case amorphous-type), which relate to some recent studies showing the role of anion rotation in the high conductivity of Li_3PS_4 [14,31]. Our hypothesis suggests that a perfectly crystalline β-Li_3PS_4 would have a low conductivity due to the absence of anion disorder, which could help understanding the RT conductivity difference between the bulk β-Li_3PS_4 (10^{-6} S.cm^{-1}) and RT-stabilized β-Li_3PS_4 (10^{-4} S.cm^{-1}).

The Le Bail analysis on the XRD pattern of 202-Li_3PS_4 (1 hour annealing) indicates the presence of a single-phase material (β-Li_3PS_4, Pnma), as illustrated in the bottom part of **Figure 10a**. When the annealing time is increased to 84 hours, the presence of crystalline ϒ-Li_3PS_4 ($Pmn2_1$ [9]) is evident in the profile-fitted XRD pattern, which has a considerably smaller lattice parameters than the ones reported by Homma et al. (a = 7.71, b = 6.54, c = 6.14 [9]). After 336 hours of annealing, the relative amount of ϒ-Li_3PS_4 is significantly increased, with larger unit-cell parameters, closer to the literature values.

As shown in the ^{31}P MAS NMR spectrum of 202-Li_3PS_4 in **Figure 10b**, β-Li_3PS_4 has amorphous-type and β-type PS_4^{3-} units. The assignment of the peak at 88.6 ppm to PS_4^{3-} units in ϒ-Li_3PS_4 (ϒ-type PS_4^{3-} units) [20] is confirmed, with a progressive increase from 17% to 49% upon increasing the annealing temperature, which is in excellent agreement with the X-ray-detected increase of the ϒ-Li_3PS_4 phase in the mixture. The crystallites of ϒ-Li_3PS_4 in 202-Li_3PS_4 may be too small to be detected by XRD. We also observe upon longer annealing duration that the amount of β-Li_3PS_4 decreases: from 66% to 52% after 84h and 50% after 336 hours. The quantities of PS_4^{3-} species in an "amorphous-type" environment decrease progressively with increasing annealing time, so that there is none detected after the longest

annealing time. These results therefore show the formation of a mixture of crystalline β- and ϒ-Li_3PS_4 at 200 °C. They also suggest that a pure ϒ phase can be obtained at the same temperature given that BM-I Li_3PS_4 is annealed for long enough. Previously, 500 °C was reported as the lowest synthesis temperature for ϒ-Li_3PS_4 [8,9,20]. Herein, we show that it can be synthesized even at 200 °C if the reagents are priorly ball-milled.

The Arrhenius plots of BM-I, β- (315-Li_3PS_4), (β+ϒ) and ϒ-Li_3PS_4 samples are shown in comparison to the literature values in **Figure 11**, in which the activation energies for ionic migration are also noted. Our findings about the transport properties of Li_3PS_4 can be summarized as follows:

i. Right after ball-milling (BM-I), we measured a high RT conductivity of 4.10^{-4} $S.cm^{-1}$, which is similar to the literature values [2,5,10,13,29,30].
ii. The conductivity increased to 9.10^{-4} $S.cm^{-1}$ after annealing the sample at 180 °C for 1 hour, which is comparable to the conductivity of cold-pressed $Li_7P_3S_{11}$ [67].
iii. Annealing at higher temperatures leads to the crystallization of β-Li_3PS_4 and gradual decrease in the conductivity. As a result, we measured a RT temperature of 8.10^{-5} $S.cm^{-1}$ in 315-Li_3PS_4. This value is smaller than the reported RT conductivity of "nanoporous" β-Li_3PS_4 (10^{-4} $S.cm^{-1}$ [16]), which could be related to its low drying (annealing) temperature (140 °C). 315-Li_3PS_4 has 3 orders of magnitude higher conductivity and a lower activation energy than "bulk" β-Li_3PS_4, which could be due to the larger domain size and the absence of mobile "amorphous-type PS_4^{3-} units" in bulk β-Li_3PS_4.
iv. While the RT conductivity of the (β+ϒ)-Li_3PS_4 sample obtained by annealing at 200 °C for 84 hours is effectively the same with 315-Li_3PS_4 (8.10^{-5} $S.cm^{-1}$), further annealing (336 hours) reduces its RT conductivity to 3.10^{-5} $S.cm^{-1}$. We correlate this decrease to the growing presence of ϒ-Li_3PS_4 in the material. Nevertheless, the phase mixture could still be

promising if its electrochemical and moisture stabilities are higher than the ones of β-Li_3PS_4, which needs to be studied.

v. The activation energies of the Li_3PS_4 samples are all within the 0.36 – 0.39 eV range (except for bulk β-Li_3PS_4 and ϒ-Li_3PS_4), implying that somehow the ionic conductivity mechanisms in these materials are similar. Relatively more distorted and dynamic PS_4^{3-} units that could play a role in the high conductivity in these materials, which could also explain the similarities in their activation energies.

vi. We also synthesized a ϒ-Li_3PS_4 sample by annealing a ball-milled Li_3PS_4 sample at 550 °C for 12 hours for comparison. We measured a very low RT conductivity of 2.10^{-7} $S.cm^{-1}$, which is similar to the value from the literature [8,9]. Relatively less dynamic ϒ-type PS_4^{3-} units could be responsible for the low conductivity of this polymorph [14].

Conclusion

In our study, we first aimed to observe if cooling breaks prevent impurity formation during the initial stages of mechanochemical synthesis of Li_3PS_4. In the absence of these cooling breaks, the quantities and the variety of impurities ($P_xS_y^{a-}$ units, polysulfides etc.) increases and the ionic conductivity of the product decreases.

Secondly, we carefully studied the changes in the variety in the $P_xS_y^{a-}$ units and the XRD pattern of BM-I Li_3PS_4 upon annealing it at different temperatures, and we correlated our findings to the modifications in its ionic conductivity. We noticed that its conductivity monotonically increases with the annealing temperature until 180 °C, which could be explained by the increase of charge carriers in its X-ray amorphous matrix. Annealing it at a higher temperature leads to a reduced conductivity and the crystallization of β-Li_3PS_4, after which the material consists of

3 distinct PS_4^{3-} units as follows: Amorphous- (located at the boundaries of β-Li_3PS_4 domains), β- and ϒ-type. The relative quantities of amorphous-type PS_4^{3-} units show correlation to β-Li_3PS_4 domain sizes and the overall conductivity of the material.

Finally, we discovered a phase mixture between β-Li_3PS_4 and ϒ-Li_3PS_4 that forms by annealing ball-milled Li_3PS_4 at 200 °C, which is the lowest temperature reported for which ϒ-Li_3PS_4 has been obtained. Increasing the relative quantity ϒ-Li_3PS_4 reduces the conductivity of the phase mixture, but it could potentially increase the moisture and/or the electrochemical stabilities of the material.

Acknowledgements

This work was supported by the Association Nationale de la Recherche et de la Technologie (ANRT) [CIFRE number 2016 / 1450]. We thank Sarah Diallo-Garcia and Stephanie Croyeau for doing some of the ^{31}P MAS NMR spectroscopy measurements.

References

[1] D. Larink, J. Ren, H. Eckert, Spectral editing based on scalar spin-spin interactions: New results on the structure of metathiophosphate glasses, Solid State Nucl. Magn. Reson. 45–46 (2012) 30–35. doi:10.1016/j.ssnmr.2012.05.001.

[2] C. Dietrich, D.A. Weber, S.J. Sedlmaier, S. Indris, S.P. Culver, D. Walter, J. Janek, W.G. Zeier, Lithium ion conductivity in Li2S–P2S5 glasses – building units and local structure evolution during the crystallization of superionic conductors Li3PS4 , Li7P3S11 and Li4P2S7, J. Mater. Chem. A. 5 (2017) 18111–18119. doi:10.1039/C7TA06067J.

[3] T. Famprikis, P. Canepa, J.A. Dawson, M.S. Islam, C. Masquelier, Fundamentals of inorganic solid-state electrolytes for batteries, Nat. Mater. 18 (2019) 1278–1291. doi:10.1038/s41563-019-0431-3.

[4] E. Ahiavi, J.A. Dawson, U. Kudu, M. Courty, M.S. Islam, O. Clemens, C. Masquelier, T. Famprikis, Mechanochemical synthesis and ion transport properties of Na3OX (X = Cl, Br, I and BH4) antiperovskite solid electrolytes, J. Power Sources. 471 (2020) 228489. doi:10.1016/j.jpowsour.2020.228489.

[5] M. Tatsumisago, S. Hama, A. Hayashi, H. Morimoto, T. Minami, New lithium ion conducting glass-ceramics prepared from mechanochemical Li2S-P2S5 glasses, Solid State Ionics. 154 (2002) 635–640. doi:10.1016/S0167-2738(02)00509-X.

[6] Q. Zhang, D. Cao, Y. Ma, A. Natan, P. Aurora, H. Zhu, Sulfide-Based Solid-State Electrolytes: Synthesis, Stability, and Potential for All-Solid-State Batteries, Adv. Mater. 31 (2019) 1–42. doi:10.1002/adma.201901131.

[7] Ö.U. Kudu, T. Famprikis, B. Fleutot, M.-D. Braida, T. Le Mercier, M.S. Islam, C. Masquelier, A review of structural properties and synthesis methods of solid electrolyte materials in the Li_2S−P_2S_5 binary system, J. Power Sources. 407 (2018) 31–43. doi:10.1016/j.jpowsour.2018.10.037.

[8] M. Tachez, J. Malugani, R. Mercier, R. Guy, Ionic conductivity of and phase transition in Li thiophosphate Li_3PS_4, Solid State Ionics. 14 (1984) 181–185. doi:http://dx.doi.org/10.1016/0167-2738(84)90097-3.

[9] K. Homma, M. Yonemura, T. Kobayashi, M. Nagao, M. Hirayama, R. Kanno, Crystal structure and phase transitions of the lithium ionic conductor Li_3PS_4, Solid State Ionics. 182 (2011) 53–58. doi:10.1016/j.ssi.2010.10.001.

[10] H. Tsukasaki, S. Mori, S. Shiotani, H. Yamamura, Ionic conductivity and crystallization process in the Li_2S–P_2S_5 glass electrolyte, Solid State Ionics. 317 (2018) 122–126. doi:10.1016/j.ssi.2018.01.010.

[11] D. Prutsch, B. Gadermaier, H. Brandstätter, V. Pregartner, B. Stanje, D. Wohlmuth, V. Epp, D. Rettenwander, I. Hanzu, H.M.R. Wilkening, Nuclear Spin Relaxation in Nanocrystalline β-Li3PS4 Reveals Low-Dimensional Li Diffusion in an Isotropic Matrix, Chem. Mater. 30 (2018) 7575–7586. doi:10.1021/acs.chemmater.8b02753.

[12] H. Stöffler, T. Zinkevich, M. Yavuz, A.-L. Hansen, M. Knapp, J. Bednarčík, S. Randau, F.H. Richter, J. Janek, H. Ehrenberg, S. Indris, Amorphous vs. Crystalline Li3PS4 : Local Structural Changes During Synthesis and Li Ion Mobility, J. Phys. Chem. C. 123 (2019) 10280–10290. doi:10.1021/acs.jpcc.9b01425.

[13] S. Shiotani, K. Ohara, H. Tsukasaki, S. Mori, R. Kanno, Pair distribution function analysis of sulfide glassy electrolytes for all-solid-state batteries: Understanding the improvement of ionic conductivity under annealing condition, Sci. Rep. 7 (2017) 6972. doi:10.1038/s41598-017-07086-y.

[14] K. Kaup, L. Zhou, A. Huq, L.F. Nazar, Impact of the Li substructure on the diffusion pathways in alpha and beta Li_3PS_4: an in situ high temperature neutron diffraction study, J. Mater. Chem. A. 8 (2020) 12446–12456. doi:10.1039/D0TA02805C.

[15] R. Mercier, J. Malugani, B. Fahys, R. Guy, Structure du Tetrathiophosphate de Lithium, Acta Crystallogr. Sect. B. (1982) 1887–1990. doi:doi:10.1107/S0567740882007535.

[16] Z. Liu, W. Fu, E.A. Payzant, X. Yu, Z. Wu, N.J. Dudney, J. Kiggans, K. Hong, A.J.

Rondinone, C. Liang, Anomalous High Ionic Conductivity of Nanoporous β-Li_3PS_4, J. Am. Chem. Soc. 135 (2013) 975–978. doi:10.1021/ja3110895.
[17] K. Homma, M. Yonemura, M. Nagao, M. Hirayama, R. Kanno, Crystal structure of high-temperature phase of lithium ionic conductor, Li_3PS_4, J. Phys. Soc. Japan. 79 (2010) 90–93. doi:10.1143/JPSJS.79SA.90.
[18] H. Stöffler, T. Zinkevich, M. Yavuz, A. Senyshyn, J. Kulisch, P. Hartmann, T. Adermann, S. Randau, F.H. Richter, J. Janek, S. Indris, H. Ehrenberg, Li+ Ion Dynamics in β-Li3PS4 Observed by NMR: Local Hopping and Long-Range Transport, J. Phys. Chem. C. 122 (2018) 15954–15965. doi:10.1021/acs.jpcc.8b05431.
[19] S. Iikubo, K. Shimoyama, S. Kawano, M. Fujii, K. Yamamoto, M. Matsushita, T. Shinmei, Y. Higo, H. Ohtani, Novel stable structure of Li_3PS_4 predicted by evolutionary algorithm under high-pressure, AIP Adv. 8 (2018) 015008. doi:10.1063/1.5011401.
[20] M. Gobet, S. Greenbaum, G. Sahu, C. Liang, Structural evolution and li dynamics in nanophase Li3PS4 by solid-state and pulsed-field gradient NMR, Chem. Mater. 26 (2014) 3558–3564. doi:10.1021/cm5012058.
[21] J.-S. Kim, W.D. Jung, S. Choi, J.-W. Son, B.-K. Kim, J.-H. Lee, H. Kim, Thermally Induced S-Sublattice Transition of Li_3PS_4 for Fast Lithium-Ion Conduction, J. Phys. Chem. Lett. 9 (2018) 5592–5597. doi:10.1021/acs.jpclett.8b01989.
[22] S. Teragawa, K. Aso, K. Tadanaga, A. Hayashi, M. Tatsumisago, Liquid-phase synthesis of a Li3PS4 solid electrolyte using N-methylformamide for all-solid-state lithium batteries, J. Mater. Chem. A. 2 (2014) 5095. doi:10.1039/c3ta15090a.
[23] N.H.H. Phuc, M. Totani, K. Morikawa, H. Muto, A. Matsuda, Preparation of Li3PS4 solid electrolyte using ethyl acetate as synthetic medium, Solid State Ionics. 288 (2015) 240–243. doi:10.1016/j.ssi.2015.11.032.
[24] H. Wang, Z.D. Hood, Y. Xia, C. Liang, Fabrication of ultrathin solid electrolyte membranes of β-Li_3PS_4 nanoflakes by evaporation-induced self-assembly for all-solid-state batteries, J. Mater. Chem. A. 4 (2016) 8091–8096. doi:10.1039/C6TA02294D.
[25] N.H.H. Phuc, K. Morikawa, M. Totani, H. Muto, A. Matsuda, Chemical synthesis of Li3PS4 precursor suspension by liquid-phase shaking, Solid State Ionics. 285 (2016) 2–5. doi:10.1016/j.ssi.2015.11.019.
[26] A. Matsuda, H. Muto, N.H.H. Phuc, Preparation of Li3PS4 Solid Electrolyte by Liquid-Phase Shaking Using Organic Solvents with Carbonyl Group as Complex Forming Medium, J. Japan Soc. Powder Powder Metall. 63 (2016) 976–980. doi:10.2497/jjspm.63.976.
[27] N.H.H. Phuc, K. Morikawa, T. Mitsuhiro, H. Muto, A. Matsuda, Synthesis of plate-like Li3PS4 solid electrolyte via liquid-phase shaking for all-solid-state lithium batteries, Ionics (Kiel). 4 (2017) 1–7. doi:10.1007/s11581-017-2035-8.
[28] J.-M. Hu, B. Wang, Y. Ji, T. Yang, X. Cheng, Y. Wang, L.-Q. Chen, Phase-field based Multiscale Modeling of Heterogeneous Solid Electrolytes: Applications to Nanoporous Li3PS4, ACS Appl. Mater. Interfaces. (2017) acsami.7b11292. doi:10.1021/acsami.7b11292.
[29] A. Hayashi, S. Hama, H. Morimoto, M. Tatsumisago, T. Minami, Preparation of Li_2S-P_2S_5 Amorphous Solid Electrolytes by Mechanical Milling, J. Am. Ceram. Soc. 84 (2001) 477–79. doi:10.1111/j.1151-2916.2001.tb00685.x.
[30] N.H.H. Phuc, H. Kazuhiro, M. Hiroyuki, M. Atsunori, High ionic conductivity of Li3−2M PS4 (M = Ca or Mg) at high temperature, Solid State Ionics. 351 (2020) 115324. doi:10.1016/j.ssi.2020.115324.
[31] J.G. Smith, D.J. Siegel, Low-temperature paddlewheel effect in glassy solid electrolytes, Nat. Commun. 11 (2020) 1483. doi:10.1038/s41467-020-15245-5.
[32] S. Lu, F. Kosaka, S. Shiotani, H. Tsukasaki, S. Mori, J. Otomo, Optimization of lithium ion conductivity of Li2S-P2S5 glass ceramics by microstructural control of crystallization kinetics, Solid State Ionics. 362 (2021) 115583. doi:10.1016/j.ssi.2021.115583.
[33] M. Takahashi, S. Yang, K. Yamamoto, K. Ohara, N.H.H. Phuc, T. Watanabe, T. Uchiyama, A. Sakuda, A. Hayashi, M. Tatsumisago, H. Muto, A. Matsuda, Y. Uchimoto, Improvement of lithium ionic conductivity of Li3PS4 through suppression of crystallization using low-boiling-point solvent in liquid-phase synthesis, Solid State Ionics. 361 (2021) 1–5. doi:10.1016/j.ssi.2021.115568.

[34] K. Yamamoto, M. Takahashi, K. Ohara, N.H.H. Phuc, S. Yang, T. Watanabe, T. Uchiyama, A. Sakuda, A. Hayashi, M. Tatsumisago, H. Muto, A. Matsuda, Y. Uchimoto, Synthesis of Sulfide Solid Electrolytes through the Liquid Phase: Optimization of the Preparation Conditions, ACS Omega. 5 (2020) 26287–26294. doi:10.1021/acsomega.0c04307.
[35] S.G.J. van Meerten, W.M.J. Franssen, A.P.M. Kentgens, ssNake: A cross-platform open-source NMR data processing and fitting application, J. Magn. Reson. 301 (2019) 56–66. doi:10.1016/j.jmr.2019.02.006.
[36] A. Cassel, B. Fleutot, M. Courty, V. Viallet, M. Morcrette, Sol-gel synthesis and electrochemical properties extracted by phase inflection detection method of NASICON-type solid electrolytes LiZr 2 (PO 4) 3 and Li 1.2 Zr 1.9 Ca 0.1 (PO 4) 3, Solid State Ionics. 309 (2017) 63–70. doi:10.1016/j.ssi.2017.07.009.
[37] K. Hayamizu, Y. Aihara, T. Watanabe, T. Yamada, S. Ito, N. Machida, NMR studies on lithium ion migration in sulfide-based conductors, amorphous and crystalline Li3PS4, Solid State Ionics. 285 (2016) 51–58. doi:10.1016/j.ssi.2015.06.016.
[38] H. Tsukasaki, S. Mori, H. Morimoto, A. Hayashi, M. Tatsumisago, Direct observation of a non-crystalline state of Li_2S–P_2S_5 solid electrolytes, Sci. Rep. 7 (2017) 4142. doi:10.1038/s41598-017-04030-y.
[39] P. Mirmira, J. Zheng, P. Ma, C. V. Amanchukwu, Importance of multimodal characterization and influence of residual Li 2 S impurity in amorphous Li 3 PS 4 inorganic electrolytes , J. Mater. Chem. A. (2021). doi:10.1039/d1ta02754a.
[40] C. Dietrich, D.A. Weber, S. Culver, A. Senyshyn, S.J. Sedlmaier, S. Indris, J. Janek, W.G. Zeier, Synthesis, Structural Characterization, and Lithium Ion Conductivity of the Lithium Thiophosphate Li2P2S6, Inorg. Chem. 56 (2017) 6681–6687. doi:10.1021/acs.inorgchem.7b00751.
[41] F. Kubel, B. Bertheville, H. Bill, Crystal structure of dilithiumsulfíde, Li2S, Z. Krist. NCS. 214 (1999) 302.
[42] A. Sakuda, A. Hayashi, M. Tatsumisago, Sulfide Solid Electrolyte with Favorable Mechanical Property for All-Solid-State Lithium Battery, Sci. Rep. 3 (2013) 2261. doi:10.1038/srep02261.
[43] R. Garcia-Mendez, J.G. Smith, J.C. Neuefeind, D.J. Siegel, J. Sakamoto, Correlating Macro and Atomic Structure with Elastic Properties and Ionic Transport of Glassy Li2S-P2S5 (LPS) Solid Electrolyte for Solid-State Li Metal Batteries, Adv. Energy Mater. 5 (2020) 1–13. doi:10.1002/aenm.202000335.
[44] P. Bonnick, K. Niitani, M. Nose, K. Suto, A high performance all solid state lithium sulfur battery with lithium thiophosphate solid, J. Mater. Chem. A. (2019) 0–6. doi:10.1039/c9ta06971b.
[45] M. Park, H.-G. Jung, W.D. Jung, S.Y. Cho, B.-N. Yun, Y.S. Lee, S. Choi, J. Ahn, J. Lim, J.Y. Sung, Y.-J. Jang, J.-P. Ahn, J.-H. Lee, H. Kim, Chemically Evolved Composite Lithium-Ion Conductors with Lithium Thiophosphates and Nickel Sulfides, ACS Energy Lett. (2017) 1740–1745. doi:10.1021/acsenergylett.7b00497.
[46] H. Muramatsu, A. Hayashi, T. Ohtomo, S. Hama, M. Tatsumisago, Structural change of Li_2S-P_2S_5 sulfide solid electrolytes in the atmosphere, Solid State Ionics. 182 (2011) 116–119. doi:10.1016/j.ssi.2010.10.013.
[47] K. Ohara, A. Mitsui, M. Mori, Y. Onodera, S. Shiotani, Y. Koyama, Y. Orikasa, M. Murakami, K. Shimoda, K. Mori, T. Fukunaga, H. Arai, Y. Uchimoto, Z. Ogumi, Structural and electronic features of binary Li2S-P2S5 glasses., Sci. Rep. 6 (2016) 21302. doi:10.1038/srep21302.
[48] J.-T. Yeon, J.-Y. Jang, J.-G. Han, J. Cho, K.T. Lee, N.-S. Choi, Raman Spectroscopic and X-ray Diffraction Studies of Sulfur Composite Electrodes during Discharge and Charge, J. Electrochem. Soc. 159 (2012) A1308–A1314. doi:10.1149/2.080208jes.
[49] Y. Aoki, K. Ogawa, T. Nakagawa, Y. Hasegawa, Y. Sakiyama, T. Kojima, M. Tabuchi, Chemical and structural changes of 70Li2S-30P2S5 solid electrolyte during heat treatment, Solid State Ionics. 310 (2017) 50–55. doi:10.1016/j.ssi.2017.08.006.
[50] B. Meyer, Elemental Sulfur, Chem. Rev. 76 (1975) 367–388.
[51] I. V. Krasnikova, M.A. Pogosova, A.O. Sanin, K.J. Stevenson, Toward Standardization of Electrochemical Impedance Spectroscopy Studies of Li-Ion Conductive Ceramics, Chem.

Mater. 32 (2020) 2232–2241. doi:10.1021/acs.chemmater.9b04899.
[52] S. Breuer, D. Prutsch, Q. Ma, V. Epp, F. Preishuber-Pflugl, F. Tietz, M. Wilkening, Separating bulk from grain boundary Li ion conductivity in the sol-gel prepared solid electrolyte Li1.5Al0.5Ti1.5(PO4)3, J. Mater. Chem. A. 3 (2015) 21343–21350. doi:10.1039/C5TA06379E.
[53] H. A. R., Simple Method to Determine Electronic and Ionic Components of the Conductivity in Mixed Conductors: A Review, Ionics (Kiel). 8 (2002) 300–313.
[54] T. Famprikis, Ö.U. Kudu, J.A. Dawson, P. Canepa, F. Fauth, E. Suard, M. Zbiri, D. Dambournet, O.J. Borkiewicz, H. Bouyanfif, S.P. Emge, S. Cretu, J.-N. Chotard, C.P. Grey, W.G. Zeier, M.S. Islam, C. Masquelier, Under Pressure: Mechanochemical Effects on Structure and Ion Conduction in the Sodium-Ion Solid Electrolyte Na_3PS_4, J. Am. Chem. Soc. 142 (2020) 18422–18436. doi:10.1021/jacs.0c06668.
[55] R. Kanno, M. Murayama, Lithium Ionic Conductor Thio-LISICON: The Li_2S-GeS_2-P_2S_5 System, J. Electrochem. Soc. 148 (2001) A742. doi:10.1149/1.1379028.
[56] A. Hayashi, S. Hama, T. Minami, M. Tatsumisago, Formation of superionic crystals from mechanically milled Li_2S-P_2S_5 glasses, Electrochem. Commun. 5 (2003) 111–114. doi:10.1016/S1388-2481(02)00555-6.
[57] A. Hayashi, S. Kama, F. Mizuno, K. Tadanaga, T. Minami, M. Tatsumisago, Characterization of Li2S-P2S5 glass-ceramics as a solid electrolyte for lithium secondary batteries, Solid State Ionics. 175 (2004) 683–686. doi:10.1016/j.ssi.2004.08.036.
[58] J. Trevey, J.S. Jang, Y.S. Jung, C.R. Stoldt, S.H. Lee, Glass-ceramic Li2S-P2S5 electrolytes prepared by a single step ball milling process and their application for all-solid-state lithium-ion batteries, Electrochem. Commun. 11 (2009) 1830–1833. doi:10.1016/j.elecom.2009.07.028.
[59] Y. Zhang, R. Chen, T. Liu, Y. Shen, Y. Lin, C.W. Nan, High Capacity, Superior Cyclic Performances in All-Solid-State Lithium-Ion Batteries Based on 78Li2S-22P2S5Glass-Ceramic Electrolytes Prepared via Simple Heat Treatment, ACS Appl. Mater. Interfaces. 9 (2017) 28542–28548. doi:10.1021/acsami.7b06038.
[60] F. Mizuno, A. Hayashi, K. Tadanaga, M. Tatsumisago, High lithium ion conducting glass-ceramics in the system Li2S-P2S5, Solid State Ionics. 177 (2006) 2721–2725. doi:10.1016/j.ssi.2006.04.017.
[61] R. Garcia-Mendez, F. Mizuno, R. Zhang, T.S. Arthur, J. Sakamoto, Effect of Processing Conditions of 75Li2S-25P2S5 Solid Electrolyte on its DC Electrochemical Behavior, Electrochim. Acta. 237 (2017) 144–151. doi:10.1016/j.electacta.2017.03.200.
[62] S. Choi, S. Lee, J. Park, W.T. Nichols, D. Shin, Facile synthesis of Li2S-P2S5 glass-ceramics electrolyte with micron range particles for all-solid-state batteries via a low-temperature solution technique (LTST), Appl. Surf. Sci. 444 (2018) 10–14. doi:10.1016/j.apsusc.2018.02.270.
[63] N.H.H. Phuc, T. Maeda, T. Yamamoto, H. Muto, A. Matsuda, Preparation of Li3PS4 – Li3PO4 Solid Electrolytes by Liquid-Phase Shaking for All-Solid-State Batteries, Electron. Mater. (2021) 39–48. doi:10.3390/electronicmat2010004.
[64] H. Eckert, Z. Zhang, J.H. Kennedy, Structural Transformation of Non-Oxide Chalcogenide Glasses. The Short-Range Order of Li_2S-P_2S_5 glasses studied by quantitative ^{31}P and $^{6,7}Li$ High-Resolution Solid-State NMR, Chem. Mater. 2 (1990) 273–279. doi:10.1021/cm00009a017.
[65] Y. Seino, M. Nakagawa, M. Senga, H. Higuchi, K. Takada, T. Sasaki, Analysis of the structure and degree of crystallisation of 70Li2S–30P2S5 glass ceramic, J. Mater. Chem. A. 3 (2015) 2756–2761. doi:10.1039/C4TA04332D.
[66] R.J. Kirkpatrick, A. Smith, S. Schramm, G. Turner, W. Yangl, Solid-State Nuclear Spectroscopy of Minerals, (1985) 29–47.
[67] Y. Seino, T. Ota, K. Takada, A. Hayashi, M. Tatsumisago, A sulphide lithium super ion conductor is superior to liquid ion conductors for use in rechargeable batteries, Energy Environ. Sci. 7 (2014) 627–631. doi:10.1039/C3EE41655K.

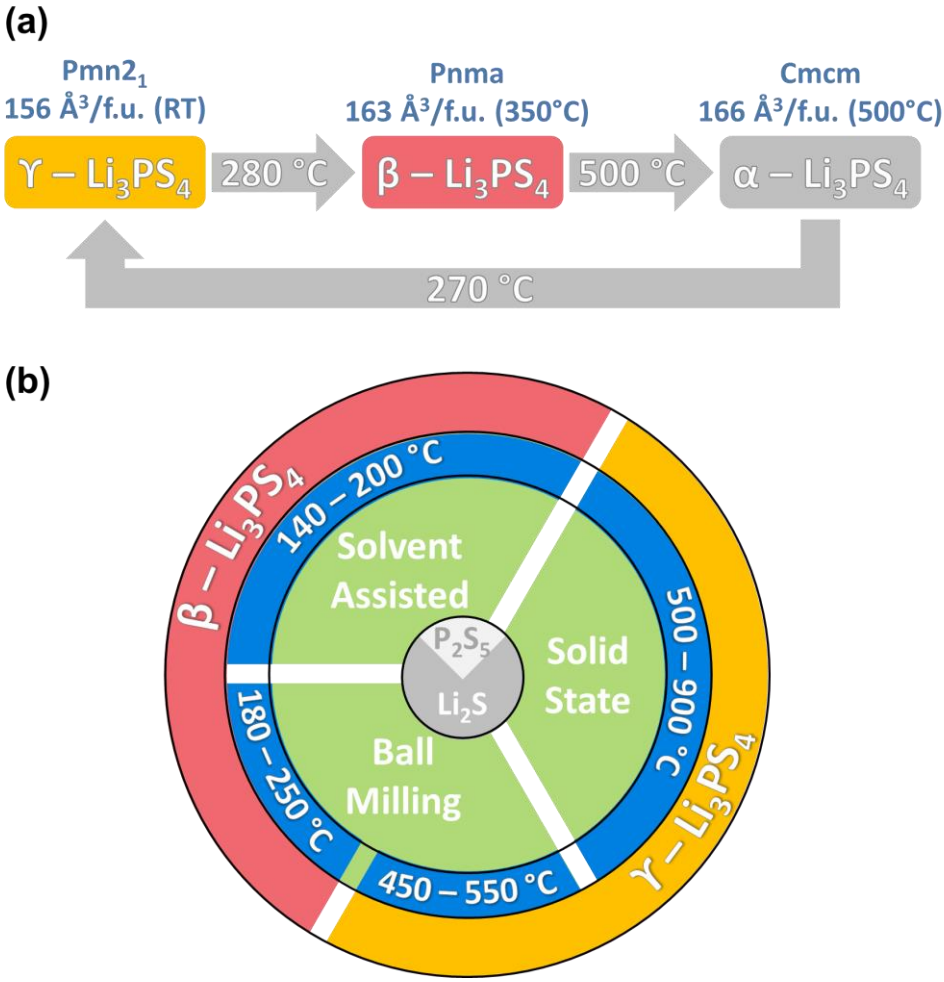

Figure 1: (Single column) a) A summary of phase transformations in ϒ-Li_3PS_4 under equilibrium conditions [9,14], and b) Different routes for the synthesis of Li_3PS_4 and the corresponding RT polymorphs

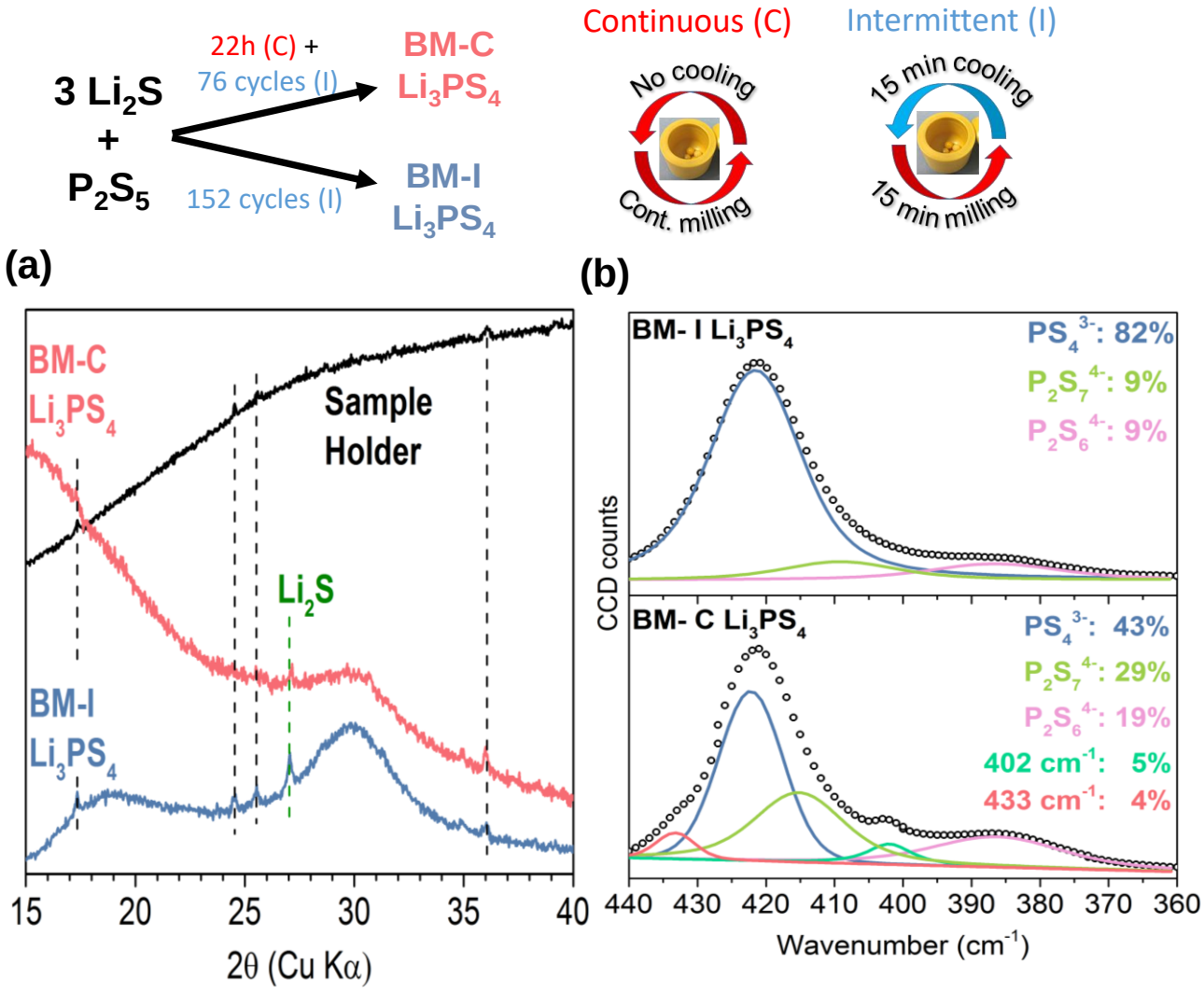

Figure 2: (Single Column) a) XRD patterns of BM-I Li_3PS_4 (collected using Cu Kα radiation) and BM-C Li_3PS_4 (collected using Co Kα radiation, then translated). b) Deconvoluted Raman spectra of BM-I and -C. In (a), the XRD patterns of the empty Be-capped sample holder is also shown to explain the presence of some diffraction peaks in the patterns of the ball-milled "Li_3PS_4" samples. The high background between 15-25° in the pattern of BM-C Li_3PS_4 is due to absence of the special blade that is used to reduce X-ray scattering at low diffraction angles in the diffractometer with Co source. In (b), the percentages indicate the relative peak areas after deconvolution. The fitting parameters are tabulated in **Table S1**

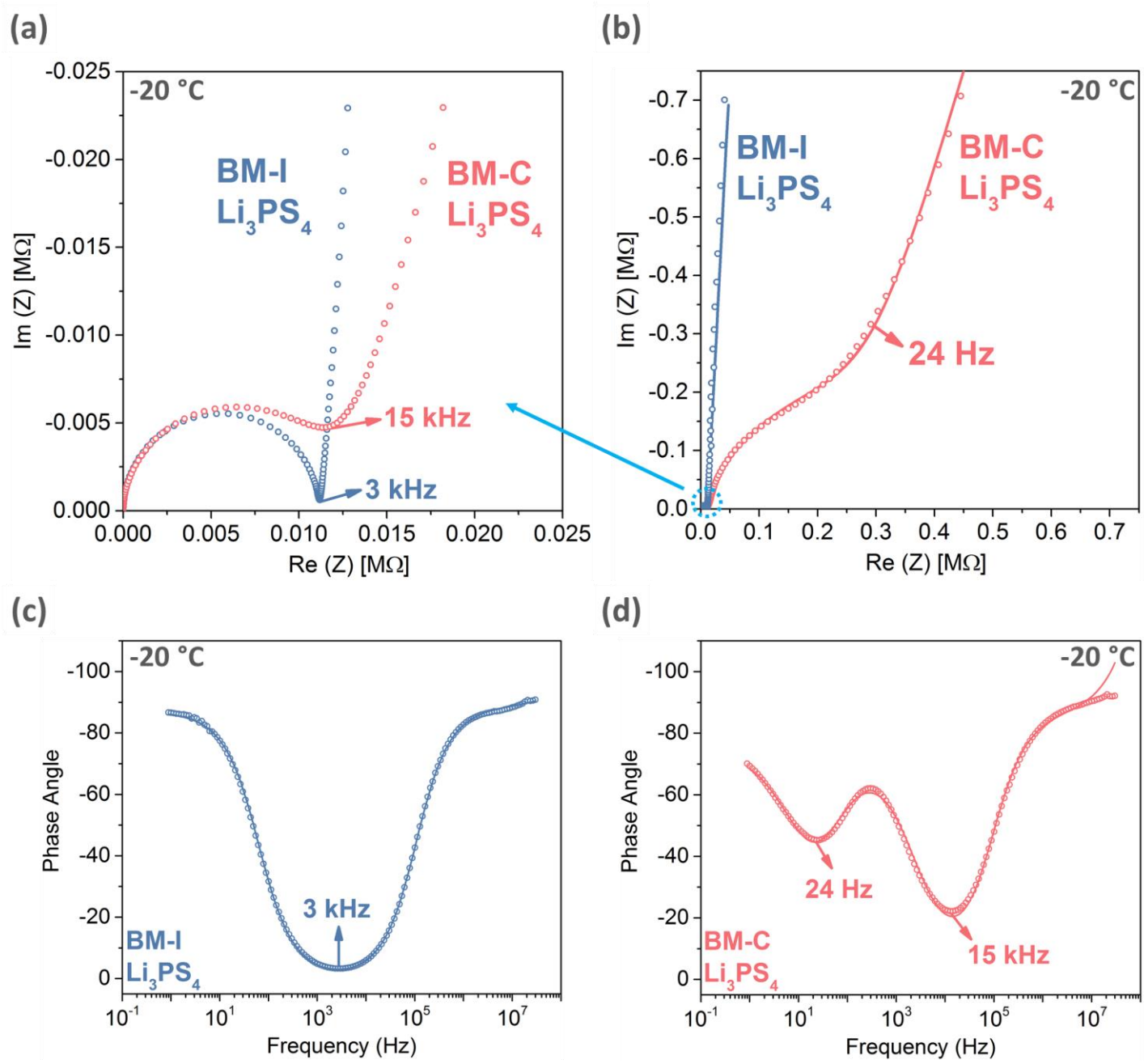

Figure 3: (double column) a) Nyquist plots of BM-I and -C Li_3PS_4 showing the high frequency region and b) full frequency region, c) Bode plot of BM-I Li_3PS_4, and BM-C Li_3PS_4. Hollow circles indicate the measured data at -20 °C, linear lines indicate the corresponding fits using Debye equivalent circuits (see **Figure S1**)

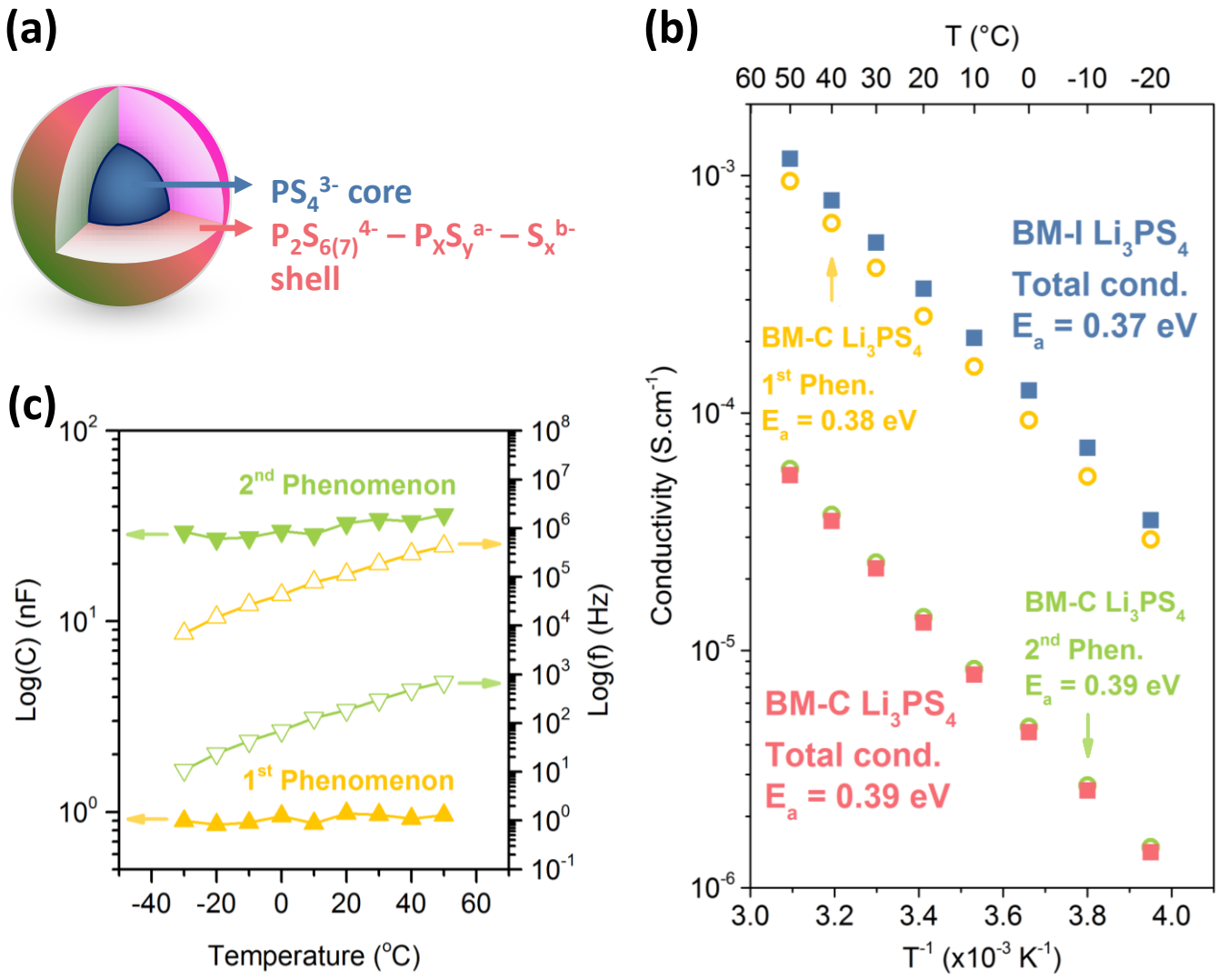

Figure 4: (double column) a) Schematic presentation of the hypothesized core-shell structure of BM-C Li_3PS_4, b) Arrhenius plots of BM-I and -C Li_3PS_4, and c) Capacitance values and cut frequencies in logarithmic scale and as a function of measurement temperature of the two conductive phenomena observed in BM-C Li_3PS_4. In (b), the 1st and the 2nd phenomenon of BM-C Li_3PS_4 are shown with hollow circles, the total conductivities of the samples are shown in filled squares

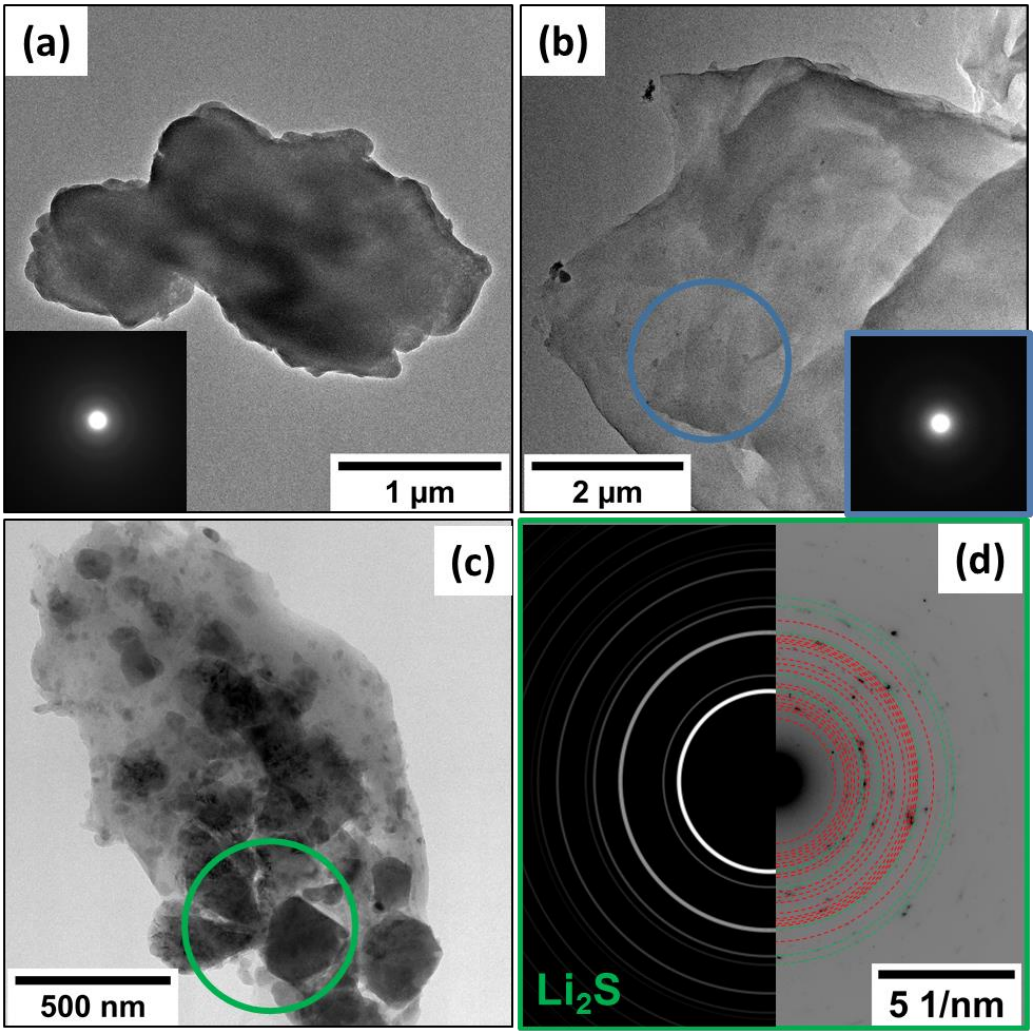

Figure 5: (single column) TEM images of a) one of the wide-spread amorphous objects and the associated SAED diffraction, b) an example of nanosized amorphous particles (in blue circle) and the associated SAED diffraction, c) amorphous objects containing crystalline particles (in green circle), and d) SAED diffraction of the crystalline objects showing the Li_2S precursor (green circles) and reaction products between Li_2S and P_2S_5 (red circles), and the simulation of Li_2S phase (white circles)

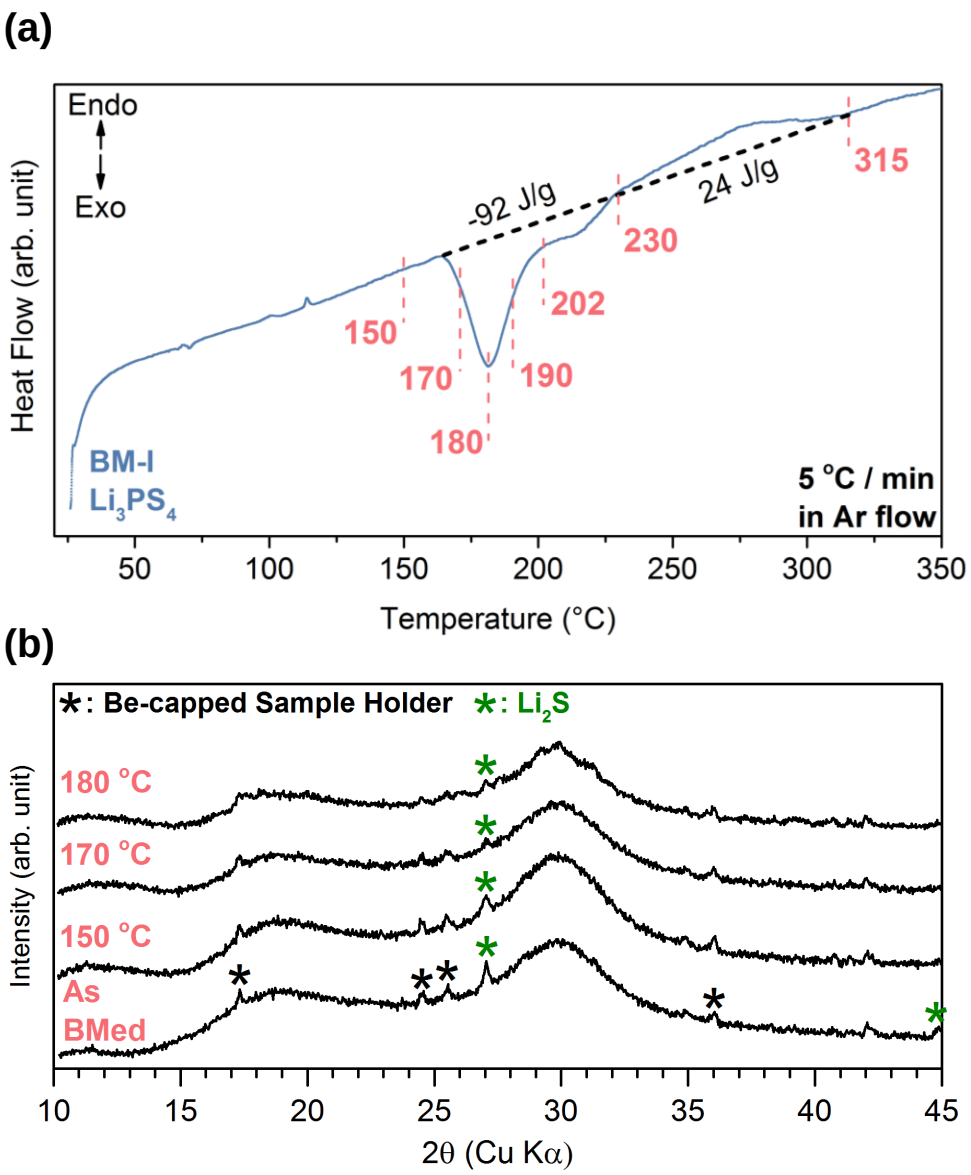

Figure 6: (single column) a) DSC data of BM-I Li_3PS_4 and b) XRD patterns of BM-I Li_3PS_4 as ball-milled, and after annealing at 150, 170 and 180 °C for 1 hour. In (a), the temperatures chosen for subsequent annealing are marked with red lines. The reaction energies are written in black.

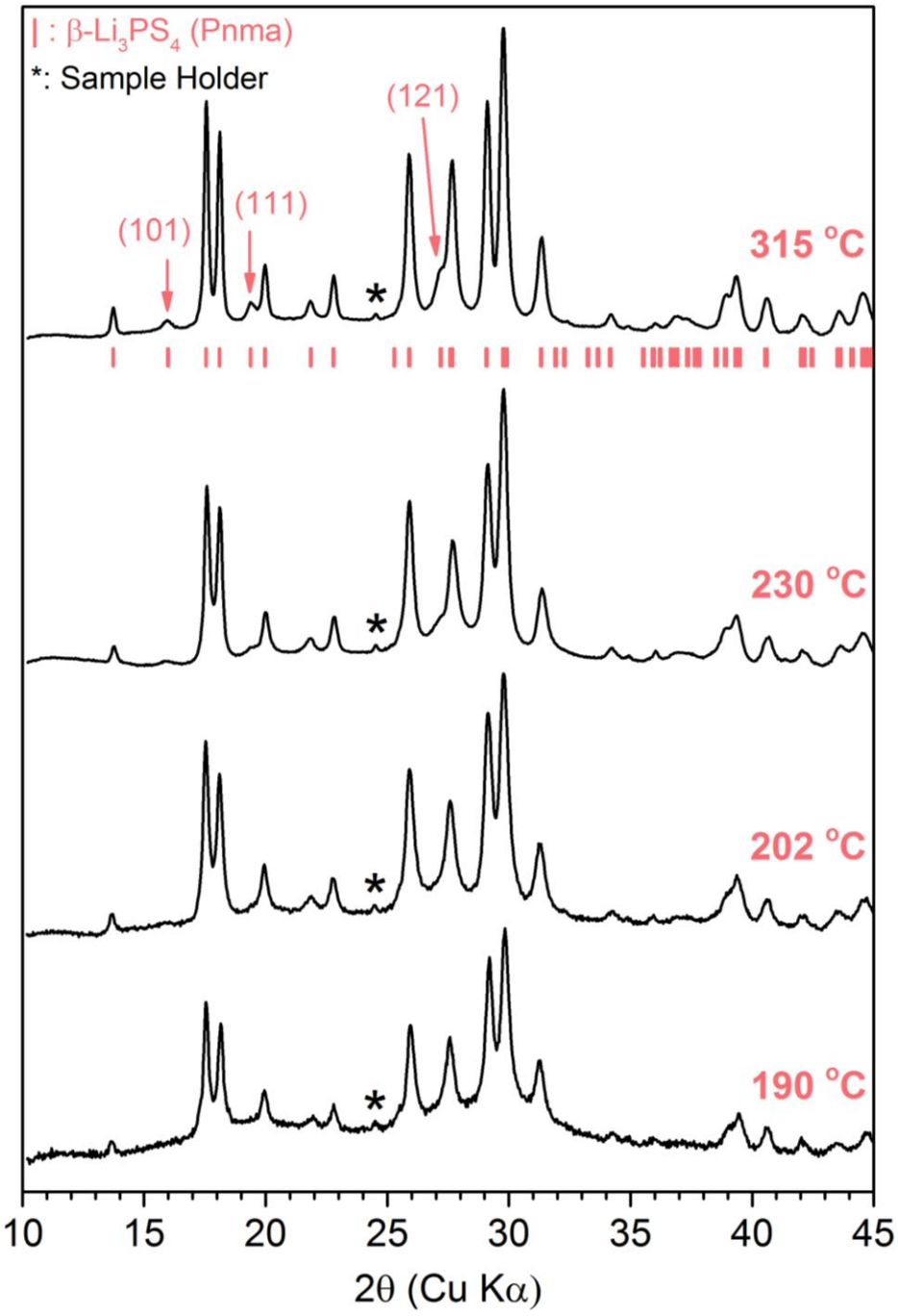

Figure 7: (single column) XRD patterns of BM-I Li_3PS_4 annealed at 190, 202, 230 and 315 °C for 1 hour. Bragg positions (Pnma) are shown in red, and the diffraction peak created by Be-capped sample holder was marked in black. The lattice parameters of these materials are listed in **Table 1**

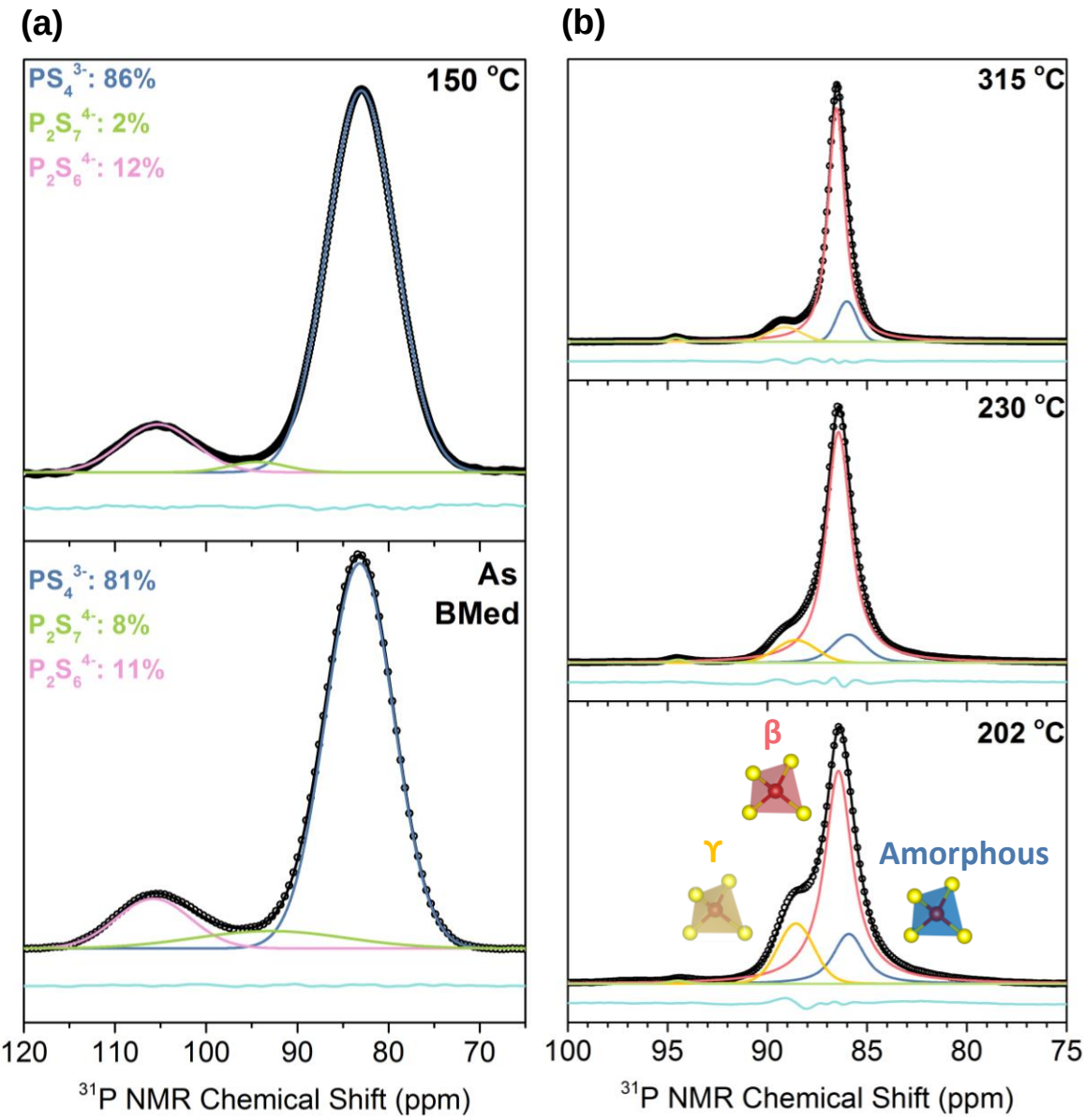

Figure 8: (Double Column) Deconvoluted ^{31}P MAS NMR spectra of a) BM-I and 150-Li_3PS_4, and b) 202-230-315-Li_3PS_4. The black circles and the black line represent the experimental data and the composite fit, respectively. The difference plot between the measured data and the fit is plotted in cyan. In (a), blue, green and pink lines are the deconvoluted signals attributed to PS_4^{3-}, $P_2S_7^{4-}$ and $P_2S_6^{4-}$ moieties, respectively. In (b), the orange, red and blue lines are the deconvoluted signals attributed to ϒ-, β- and amorphous-type PS_4^{3-} moieties, respectively. The fitting parameters of (a) are shown in **Table S2.** The relative ratios between the structural moieties and the fitting parameters of (b) are shown in **Tables 2** and **S3**, respectively.

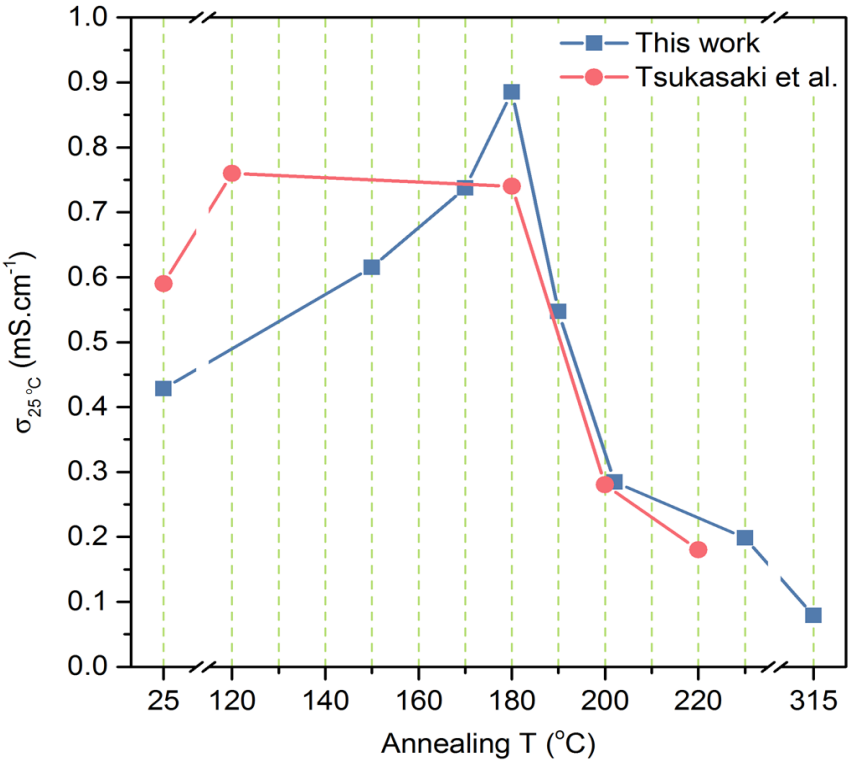

Figure 9: (single column) Ionic conductivities (at 25 °C) of ball-milled and subsequently annealed Li_3PS_4 samples. Blue color represents the data obtained in this work, red color represents the data obtained from ball-milled and subsequently annealed Li_3PS_4 samples by Tsukasaki et al. [10].

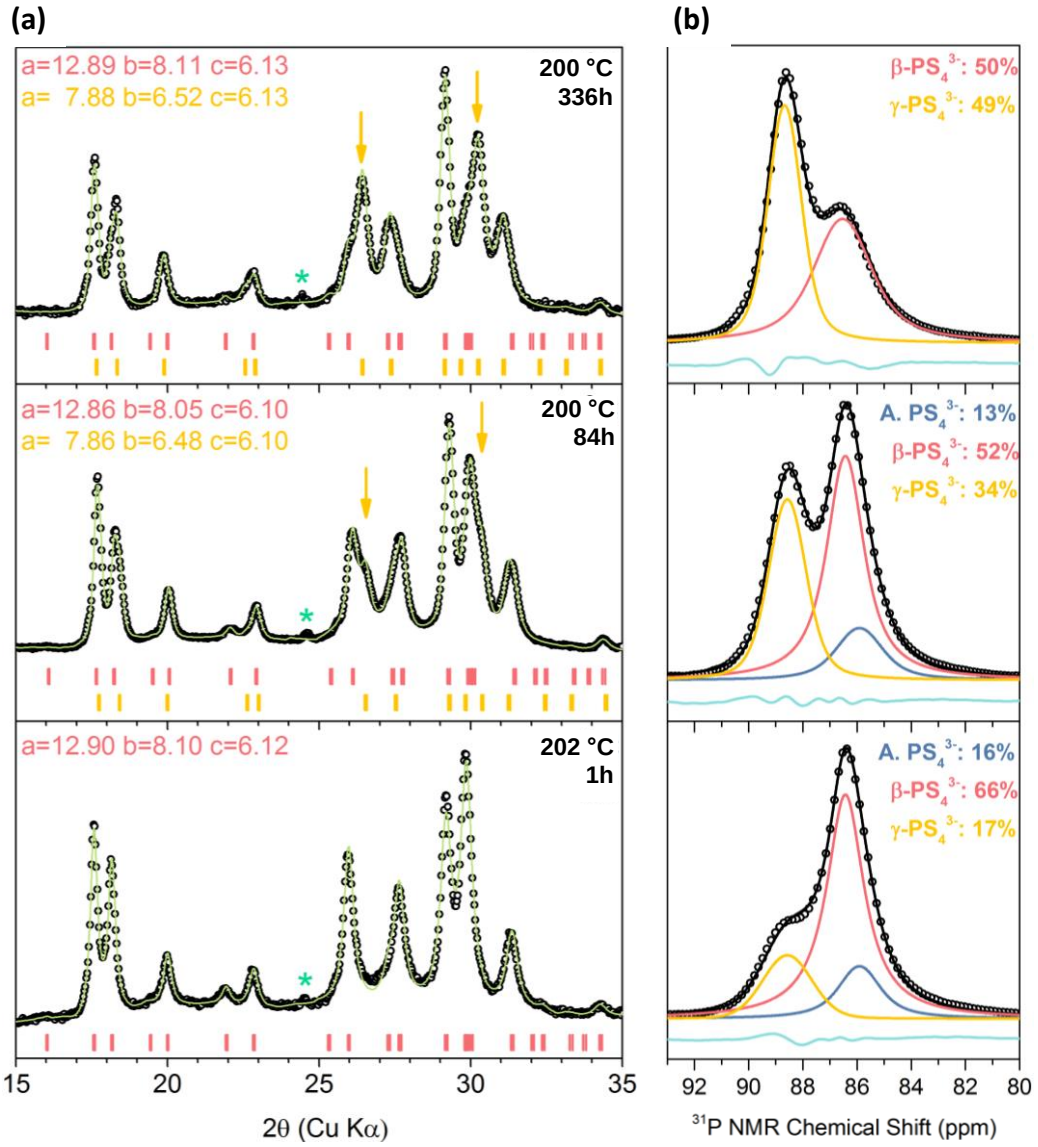

Figure 10: (Double column) a) Profile fitted XRD patterns of, and b) ^{31}P MAS NMR spectra of BM-I Li_3PS_4 annealed at 200 and 202 °C for 1, 84 and 336 hours, fitted using 3 Voigt peaks. In (a), red text and bars indicate the lattice parameters and Bragg positions of β-Li_3PS_4 whereas the orange ones stand for ϒ-Li_3PS_4. The asterisk marks the reflection produced by the Be-capped sample holder. In (b), the black circles and the black line represent the experimental data and the composite fit, respectively. the orange, red and blue lines are the deconvoluted signals attributed to ϒ-, β- and amorphous-type PS_4^{3-} moieties, respectively. The difference plot between the measured data and the fit is plotted in cyan. The fitting parameters are listed in **Table S3.** The fits and the fitting parameters assuming only 2 distinct PS_4^{3-} species, which produce lower consistency with the observed data, are also shown for comparison in **Table S4** and **Figure S3**.

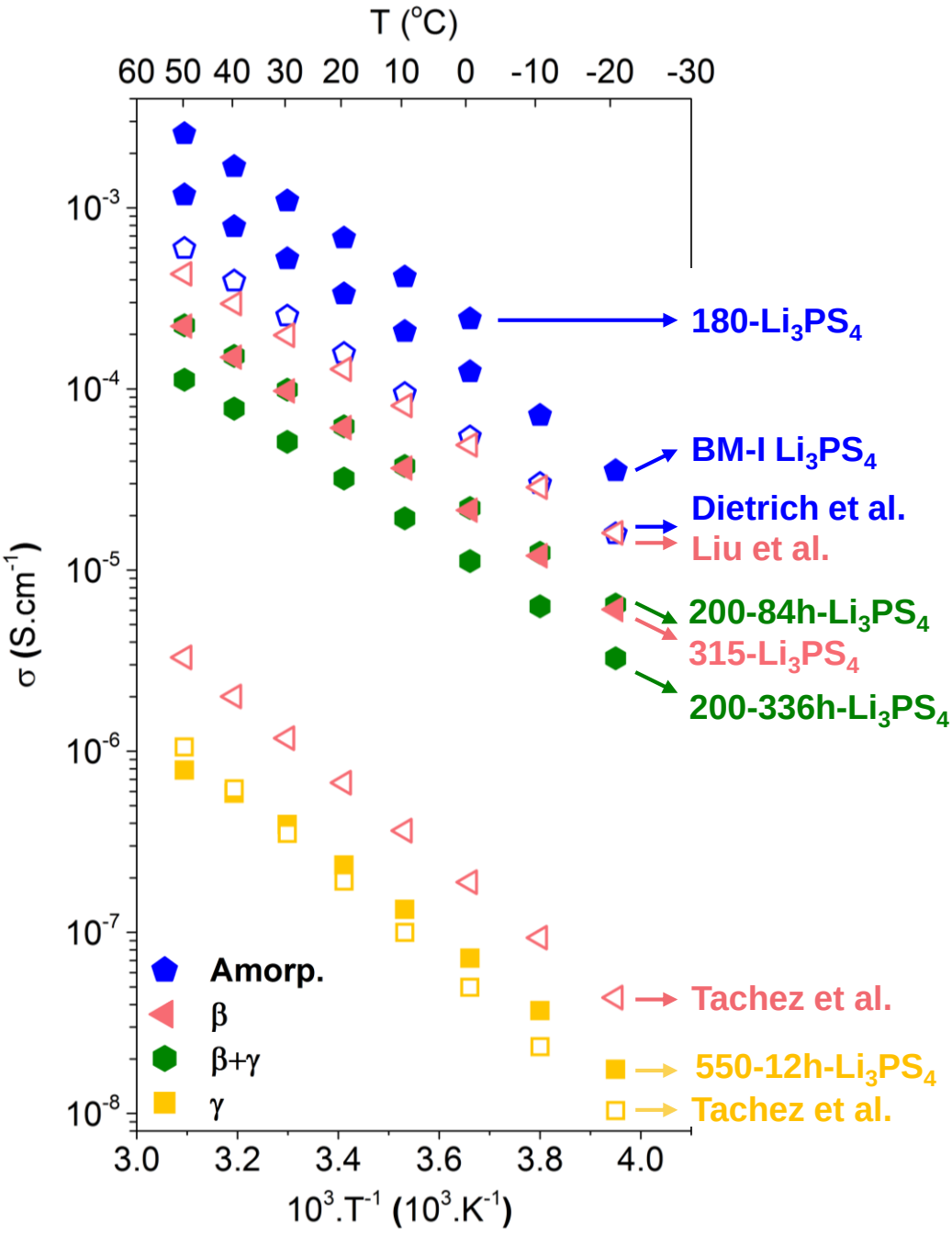

Figure 11: (single or double column?) Arrhenius plots of BM-I, β-(315-Li_3PS_4), (β+ϒ) and ϒ-Li_3PS_4 samples (filled symbols) in comparison to the literature data (hollow symbols). The activation energies from up to down are 0.38, 0.37, 0.39, 0.36, 0.38, 0.38, 0.38, 0.46, 0.42, 0.49 eV. The afore-mentioned references are as follows: Dietrich et al. [2], Liu et al. [16], Tachez et al. [8]

Supporting Information for:

Overlooked structural details in ball-milled Li_3PS_4: variety in thiophosphate building blocks and correlation to ion transport

Ömer Ulaş Kudu [a,d], Theodosios Famprikis [a,c], Sorina Cretu [a], Benjamin Porcheron [b,e], Elodie Salager [b,e], Arnaud Demortiere [a], Matthieu Courty [a,b], Virginie Viallet [a,b], Thierry Le Mercier [d], Benoit Fleutot [a,b], Marc-David Braida [d], Christian Masquelier [a,b,c*]*

[a] Laboratoire de Réactivité et de Chimie des Solides (UMR CNRS 7314), Université de Picardie Jules Verne, 33 rue Saint Leu, 80039 Amiens Cedex, France

[b] Réseau sur le Stockage Électrochimique de l'Énergie (RS2E), FR CNRS 3459, 80039 Amiens, France

[c] ALISTORE European Research Institute, FR CNRS 3104, 80039 Amiens Cedex, France

[d] Solvay R&I, 52 rue de la Haie Coq, 93306 Aubervilliers, France

[e] CNRS, CEMHTI UPR 3079, Université d'Orléans, Orléans, France

***Corresponding Authors**

ulaskudu@gmail.com (U.K.)
christian.masquelier@u-picardie.fr (C.M.)

Table S1: The fitting parameters of deconvoluted Raman spectra of BM-I and -C Li_3PS_4 using Voigt function. FWHH stands for full width at half height

	Assigned Unit	Peak Center	FWHH		Assigned Unit	Peak Center	FWHH
BM-I Li_3PS_4	$P_2S_6^{4-}$	387	14.9	**BM-C Li_3PS_4**	$P_2S_6^{4-}$	386	15.0
	$P_2S_7^{4-}$	409	12.7		?	402	2.3
	PS_4^{3-}	422	10.8		$P_2S_7^{4-}$	415	10.7
	-	-	-		PS_4^{3-}	422	10.6
	-	-	-		?	433	5.6

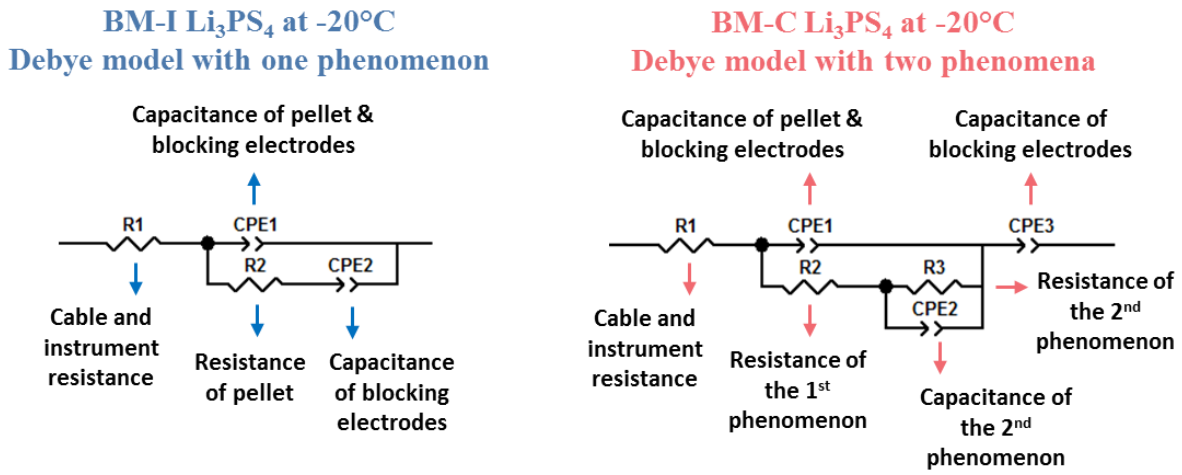

Figure S1: The Debye equivalent circuits used for fitting the impedance data of BM-I and -C Li_3PS_4 [1]

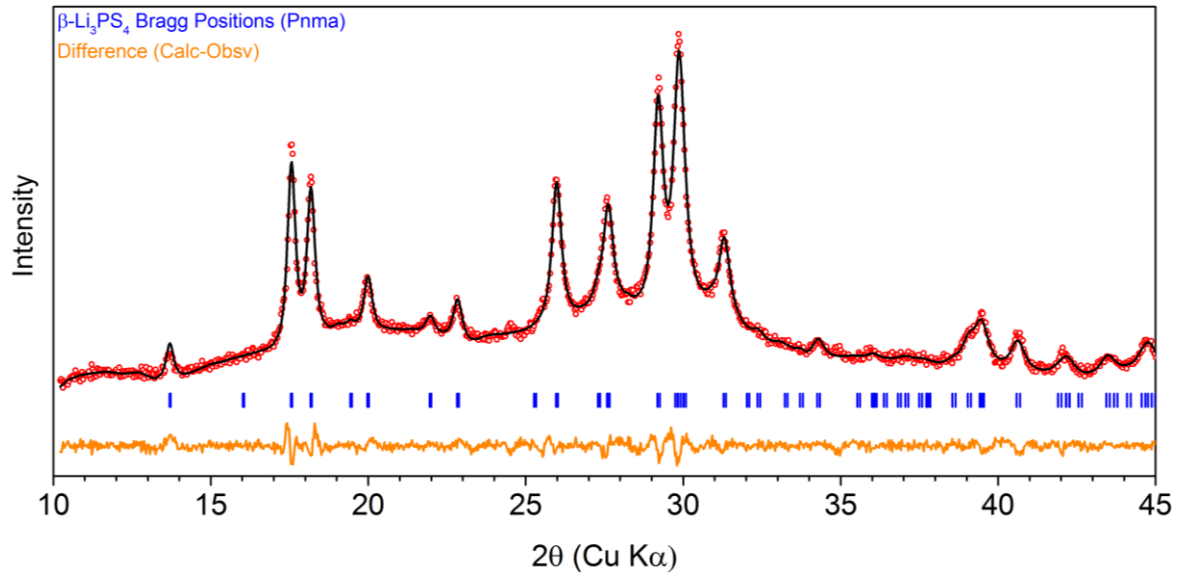

Figure S2: Profile fitted XRD pattern of 190-Li_3PS_4. Red circles indicate the collected data; black and orange lines stand for the Le Bail fit and the difference plot, respectively. Blue sticks indicate the fitted Bragg positions for the Pnma space group.

Table S2: The fitting parameters of deconvoluted ^{31}P MAS NMR spectra of BM-I- and 150-Li_3PS_4 to 3 distinct components. **A.**, **G.** and **L.** stand for amorphous-type[-], Gaussian and Lorentzian, respectively.

	Assigned unit	Shift (ppm)	Peak width (Hz, L.)	Peak width (Hz, G.)	Relative signal ratio (%)
150-Li_3PS_4	A. PS_4^{3-}	83.0	0	1429	86
	A. $P_2S_7^{4-}$	94.4	0	1185	2
	A. $P_2S_6^{4-}$	105.3	0	1539	12

	Assigned unit	Shift (ppm)	Peak width (Hz, L.)	Peak width (Hz, G.)	Relative signal ratio (%)
BM-I-Li_3PS_4	A. PS_4^{3-}	83.2	0	1423	81
	A. $P_2S_7^{4-}$	93.0	0	3157	8
	A. $P_2S_6^{4-}$	105.8	0	1559	11

Table S3: The fitting parameters of deconvoluted ^{31}P MAS NMR spectra of 202-, 230-, 315-Li_3PS_4, BM-Li_3PS_4 annealed at 200 °C for 84 hours and for 336 hours, using 3 distinct PS_4^{3-} components. **A. PS_4^{3-}**, **G.** and **L.** are the abbreviations for amorphous-type PS_4^{3-}, Gaussian and Lorentzian, respectively.

	Assigned unit	Shift (ppm)	Peak width (Hz, L.)	Peak width (ppm, G.)	Relative signal ratio (%)
202-Li_3PS_4	A. PS_4^{3-}	85.9	224	145	16
	β. PS_4^{3-}	86.4	270	0	66
	ϒ. PS_4^{3-}	88.6	39	326	17
	$P_2S_7^{4-}$	94.5	0	184	0
	$P_2S_7^{4-}$	96.7	0	286	0

	Assigned unit	Shift (ppm)	Peak width (Hz, L.)	Peak width (ppm, G.)	Relative signal ratio (%)
230-Li_3PS_4	A. PS_4^{3-}	85.9	119	254	11
	β. PS_4^{3-}	86.4	214	74	80
	ϒ. PS_4^{3-}	88.6	0	392	9
	$P_2S_7^{4-}$	94.5	0	146	0
	$P_2S_7^{4-}$	96.7	-	-	-

	Assigned unit	Shift (ppm)	Peak width (Hz, L.)	Peak width (ppm, G.)	Relative signal ratio (%)
315-Li_3PS_4	A. PS_4^{3-}	85.9	0	193	12
	β. PS_4^{3-}	86.4	141	58	80
	ϒ. PS_4^{3-}	89.1	0	326	7
	$P_2S_7^{4-}$	94.5	0	140	1
	$P_2S_7^{4-}$	96.7	-	-	-

	Assigned unit	Shift (ppm)	Peak width (Hz, L.)	Peak width (ppm, G.)	Relative signal ratio (%)
200 °C for 84h	A. PS_4^{3-}	85.9	196	208	13
	β. PS_4^{3-}	86.4	230	97	52
	ϒ. PS_4^{3-}	88.6	91	213	34
	$P_2S_7^{4-}$	94.5	0	184	0
	$P_2S_7^{4-}$	96.7	0	286	1

	Assigned unit	Shift (ppm)	Peak width (Hz, L.)	Peak width (ppm, G.)	Relative signal ratio (%)
200 °C for 336h	A. PS_4^{3-}	85.9	0	0	0
	β. PS_4^{3-}	86.4	279	231	50
	ϒ. PS_4^{3-}	88.6	91	184	49
	$P_2S_7^{4-}$	94.5	-	-	-
	$P_2S_7^{4-}$	96.7	0	286	1

Table S4: The fitting parameters of deconvoluted ^{31}P MAS NMR spectra of 202-, 230- and 315-Li_3PS_4, BM-Li_3PS_4 annealed at 200 °C for 84 hours and for 336 hours, using to 2 distinct PS_4^{3-} components. **A. PS_4^{3-}**, **G.** and **L.** are the abbreviations for amorphous-type PS_4^{3-}, Gaussian and Lorentzian, respectively.

	Assigned unit	Shift (ppm)	Peak width (Hz, L.)	Peak width (ppm, G.)	Relative signal ratio (%)
202-Li_3PS_4	β. PS_4^{3-}	86.4	285	51	84
	ϒ. PS_4^{3-}	88.6	48	294	15
	$P_2S_7^{4-}$	94.5	0	164	0
	$P_2S_7^{4-}$	96.7	0	278	0

	Assigned unit	Shift (ppm)	Peak width (Hz, L.)	Peak width (ppm, G.)	Relative signal ratio (%)
230-Li_3PS_4	β. PS_4^{3-}	86.4	218	96	91
	ϒ. PS_4^{3-}	88.6	0	408	9
	$P_2S_7^{4-}$	94.5	0	138	0
	$P_2S_7^{4-}$	96.7	-	-	-

	Assigned unit	Shift (ppm)	Peak width (Hz, L.)	Peak width (ppm, G.)	Relative signal ratio (%)
315-Li_3PS_4	β. PS_4^{3-}	86.4	146	77	94
	ϒ. PS_4^{3-}	89.3	0	261	5
	$P_2S_7^{4-}$	94.5	0	130	1
	$P_2S_7^{4-}$	96.7	-	-	-

	Assigned unit	Shift (ppm)	Peak width (Hz, L.)	Peak width (ppm, G.)	Relative signal ratio (%)
200 °C for 84h	β. PS_4^{3-}	86.4	250	115	68
	ϒ. PS_4^{3-}	88.6	84	207	32
	$P_2S_7^{4-}$	94.5	0	164	0
	$P_2S_7^{4-}$	96.7	0	278	1

	Assigned unit	Shift (ppm)	Peak width (Hz, L.)	Peak width (ppm, G.)	Relative signal ratio (%)
200 °C for 336h	β. PS_4^{3-}	86.4	245	262	48
	ϒ. PS_4^{3-}	88.5	97	185	51
	$P_2S_7^{4-}$	94.5	-	-	-
	$P_2S_7^{4-}$	96.7	0	278	1

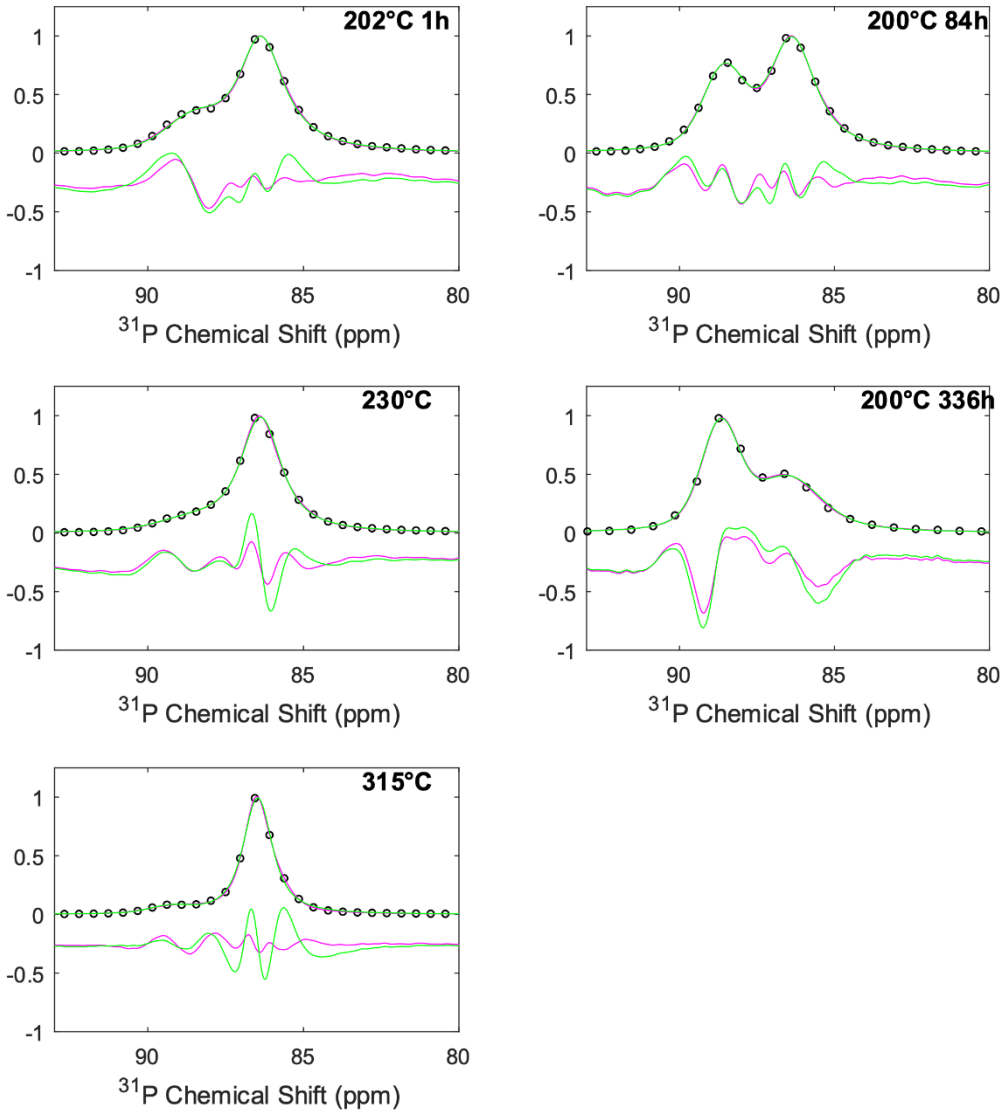

Figure S3: Fitted ^{31}P MAS NMR spectra of the 5 samples: 202-, 230-, 315-Li_3PS_4.and BM-Li_3PS_4 annealed at 200 °C for 84 hours and for 336 hours. The black circles stand for the experimental data, the magenta line shows the composite fit with 3 components; together with the difference plot below (scale x10). The corresponding data are shown in green for the 2-component fit.

References

[1] H. A. R., Simple Method to Determine Electronic and Ionic Components of the Conductivity in Mixed Conductors: A Review, Ionics (Kiel). 8 (2002) 300–313.

[2] S. J. Rettig; J. Trotter, Refinement of the structure of orthorhombic sulfur, α-S8, Acta Crystallogr. Sect. C Cryst. Struct. Commun. C43 (1987) 2260–2262.